

## Supporting Information for

# Ordered Interfacial Domain Expansion Catalysis Enhances Hydrogen Evolution for Proton Exchange Membrane Electrolysis

Ming-Rong Qu<sup>1†</sup>, Yu-Xiao Cheng<sup>2†</sup>, Si-Hua Feng<sup>3†</sup>, Jie Xu<sup>4</sup>, Jia-Kang Yao<sup>2</sup>, Wen-Sheng Yan<sup>3</sup>, Sheng Zhu<sup>1↑</sup>, Liang Cao<sup>2↑</sup>, Rui Wu<sup>1↑</sup> & Shu-Hong Yu<sup>1.5↑</sup>

<sup>1</sup>New Cornerstone Science Laboratory, Department of Chemistry, Institute of Biomimetic Materials & Chemistry, Anhui Engineering Laboratory of Biomimetic Materials, Division of Nanomaterials & Chemistry, Hefei National Research Center for Physical Sciences at the Microscale, University of Science and Technology of China, Hefei 230026, China.

<sup>2</sup>Institute of Catalysis, Department of Chemistry, Zhejiang University, Hangzhou 310058, China.

<sup>3</sup>National Synchrotron Radiation Laboratory, University of Science and Technology of China, 230026 Hefei, Anhui, China.

<sup>4</sup>College of Chemistry and Materials Engineering, Wenzhou University, Wenzhou 325035, China.

<sup>5</sup>Institute of Innovative Materials (I2M), Department of Chemistry, Department of Materials Science and Engineering, Southern University of Science and Technology, Shenzhen 518055, China.

†These authors contributed equally to this work.

↑Correspondence to: [zhusheng@shiep.edu.cn](mailto:zhusheng@shiep.edu.cn), [wuruistc@mail.ustc.edu.cn](mailto:wuruistc@mail.ustc.edu.cn), [liangcao@zju.edu.cn](mailto:liangcao@zju.edu.cn), [shyu@ustc.edu.cn](mailto:shyu@ustc.edu.cn) or [yush@sustech.edu.cn](mailto:yush@sustech.edu.cn)

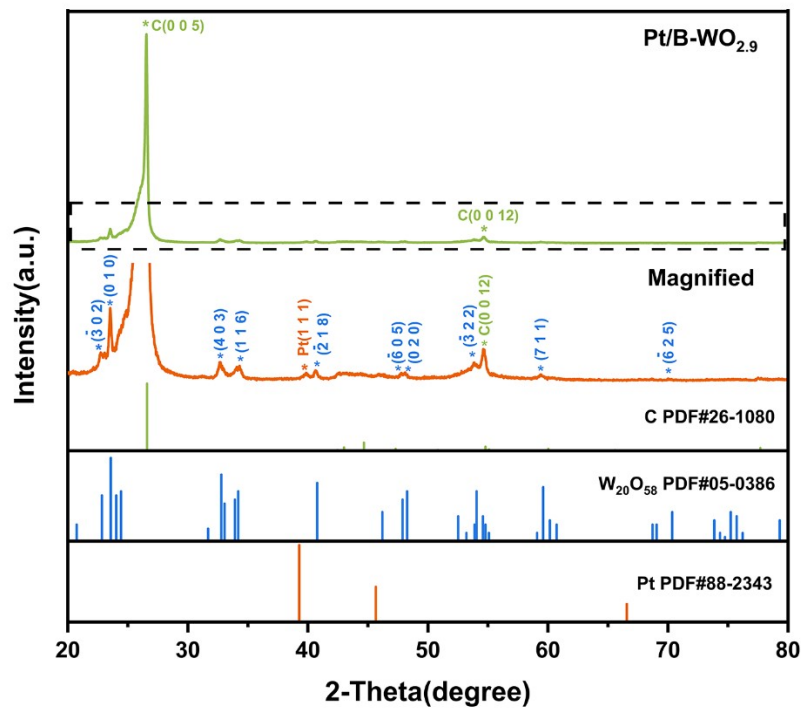


**Figure S1.** XRD patterns of Pt/B-WO<sub>2.9</sub>. Green is the total profile; orange is the magnified profile.

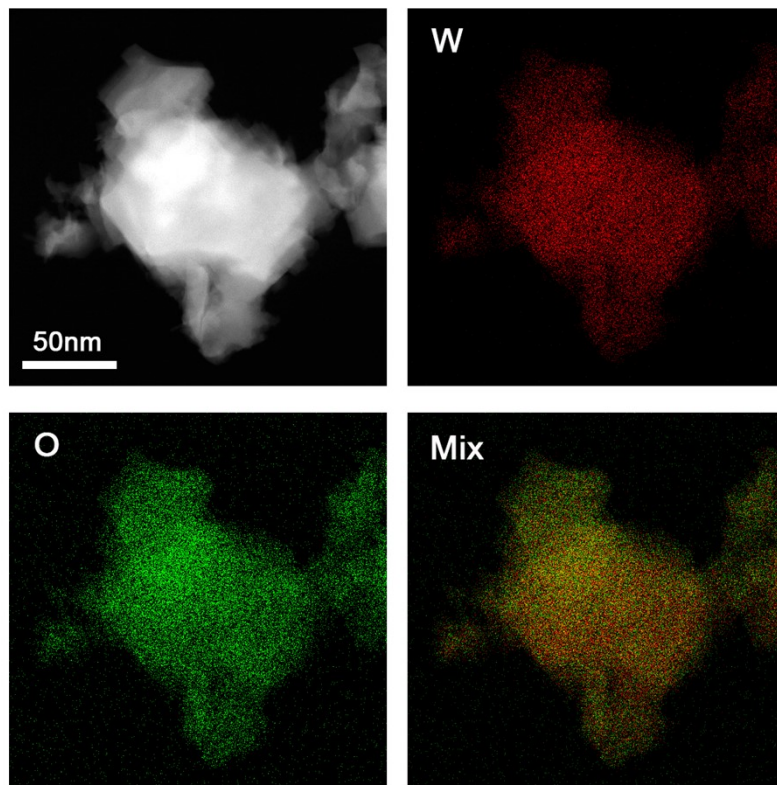


**Figure S2.** HAADF and EDS mapping images of  $\text{WO}_{2.9}$ .

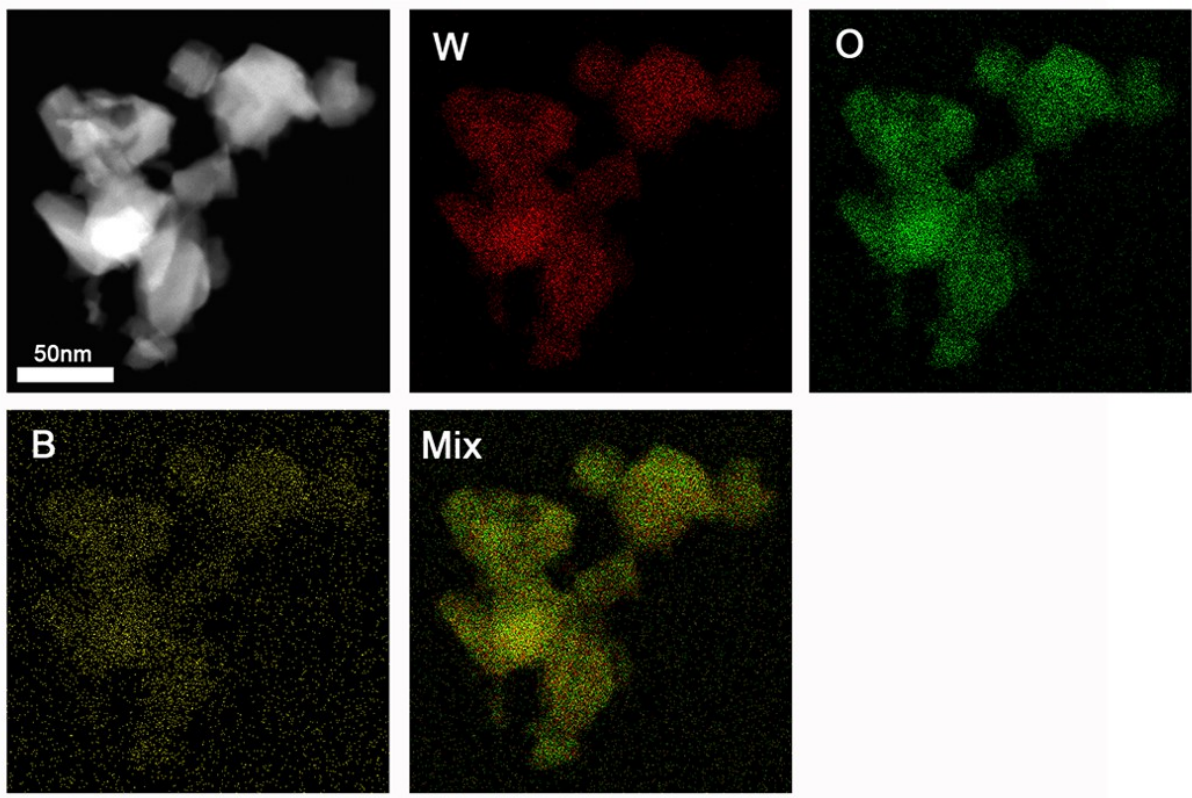


**Figure S3.** HAADF and EDS mapping images of B-WO<sub>2.9</sub>.

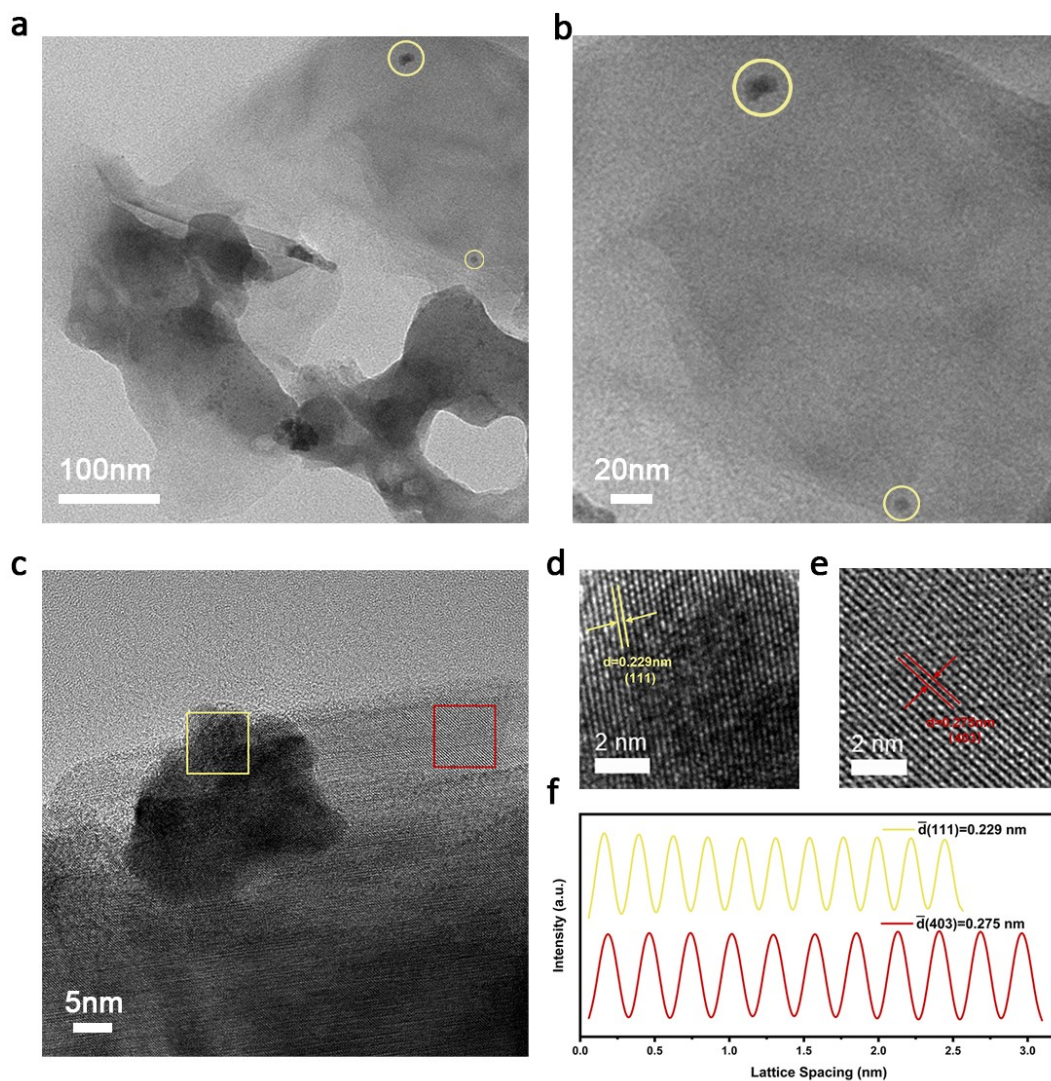


**Figure S4.** Microscopic images. (a-b) TEM images of Pt/B-WO<sub>2.9</sub>, Pt is surrounded by yellow circles. (c) HRTEM images of Pt/B-WO<sub>2.9</sub>. (d) HRTEM of Pt in (c) indicated by yellow box. (e) HRTEM of B-WO<sub>2.9</sub> in (c) indicated by red box. (f) The integrated pixel intensities of spacings along Pt (111) and WO<sub>2.9</sub> (403) facets.

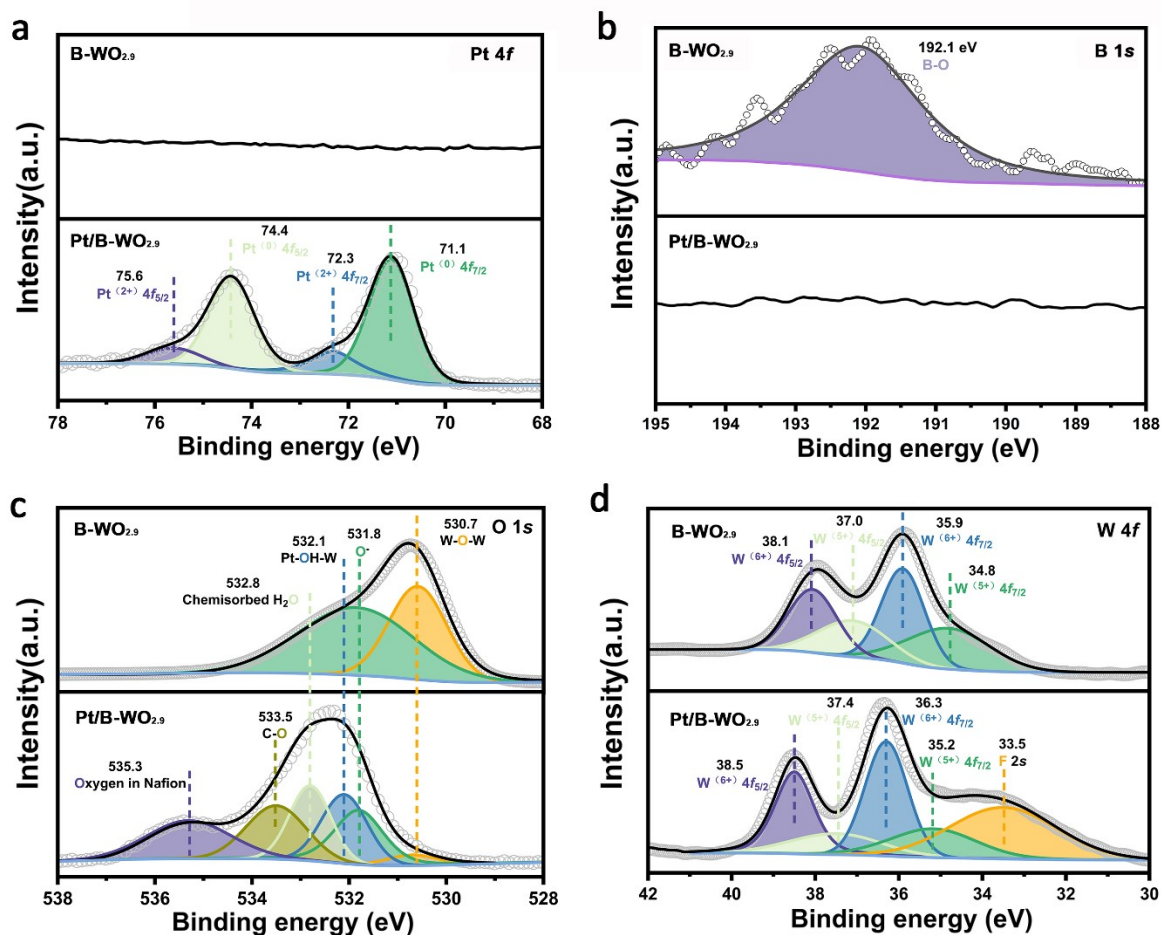


**Figure S5.** Detailed XPS survey of Pt/B-WO<sub>2.9</sub> and B-WO<sub>2.9</sub>, showing the core-level regions of Pt 4f (a), B 1s (b), O 1s (c) and W 4f (d). For the O 1s spectra further revealed peaks at 530.7 eV and 531.8 eV for B-WO<sub>2.9</sub>, corresponding to the bridge oxygen (e.g. W-O-W) and terminal oxygen (O<sup>-</sup>), respectively<sup>1</sup>. For Pt/B-WO<sub>2.9</sub>, additional peaks were observed at 532.1, 532.8, 533.5 and 535.3 eV, attributed to protonated Pt-OH-W bonds<sup>2</sup>, chemisorbed H<sub>2</sub>O<sup>3</sup>, C-O bond from carbon paper<sup>4</sup> and oxygen species in Nafion<sup>5</sup>, respectively. The W 4f spectra (Figure 1g) showed peaks at 34.8 and 37.0 eV corresponding to W<sup>(5+)</sup> 4f<sub>7/2</sub> and W<sup>(5+)</sup> 4f<sub>5/2</sub>, respectively, and peaks at 35.9 and 38.1 eV are W<sup>(6+)</sup> 4f<sub>7/2</sub> and W<sup>(6+)</sup> 4f<sub>5/2</sub>, respectively<sup>6,7</sup>. In addition, a new peak appears at 33.5 eV in Pt/B-WO<sub>2.9</sub>, assigning to F 2s peak caused by Nafion<sup>8</sup>.

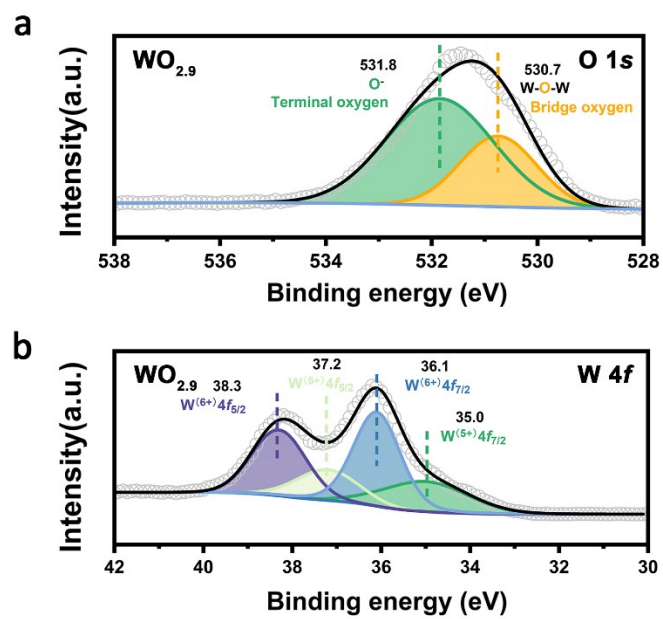


**Figure S6.** Detailed XPS survey of  $\text{WO}_{2.9}$ , showing the core-level regions of O 1s (a) and W 4f (b).

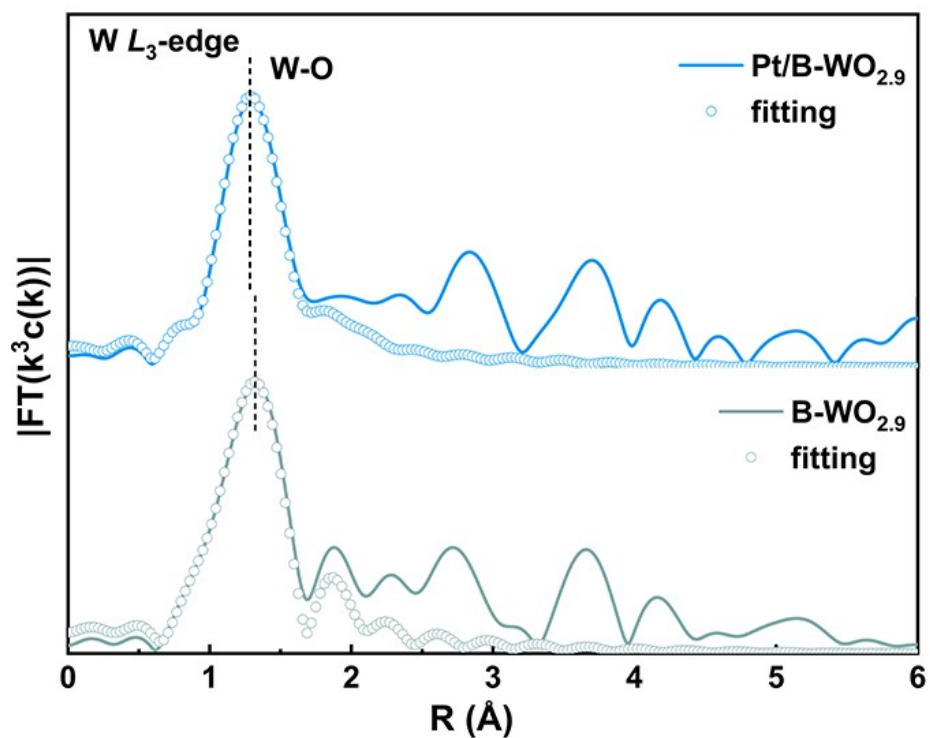


**Figure S7.**  $k_3$ -weighted Fourier transforms of EXAFS spectra. Tungsten  $L_3$  edge of the Pt/B-WO<sub>2.9</sub> (above) and B-WO<sub>2.9</sub> (below). Experimental data and fitting data are solid and dotted lines, respectively.

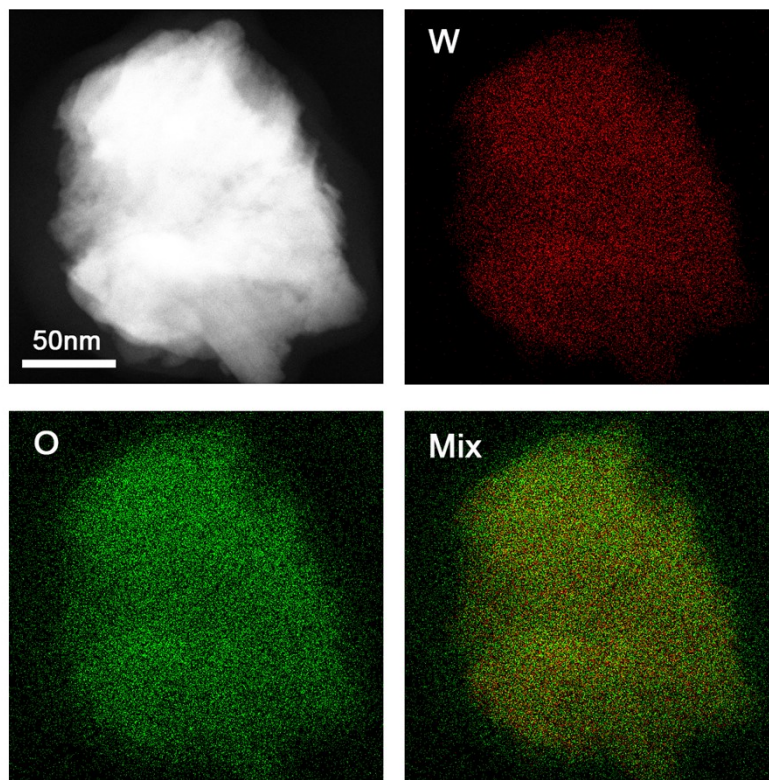


**Figure S8.** HAADF and EDS mapping images of A-WO<sub>2.9</sub> (Pt-WO<sub>2.9</sub>).

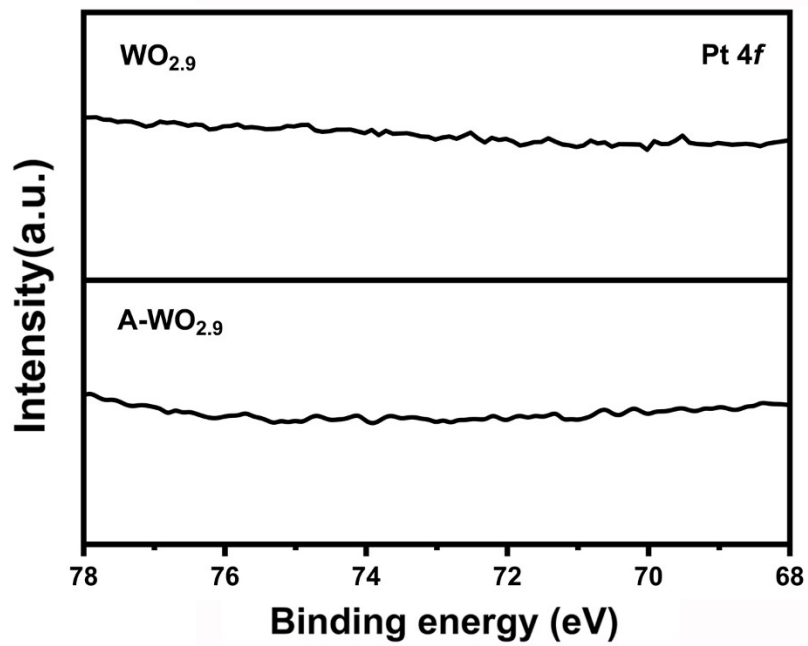


**Figure S9.** Detailed XPS survey of Pt 4f core-level region spectra of  $\text{WO}_{2.9}$  and Activated- $\text{WO}_{2.9}$ .

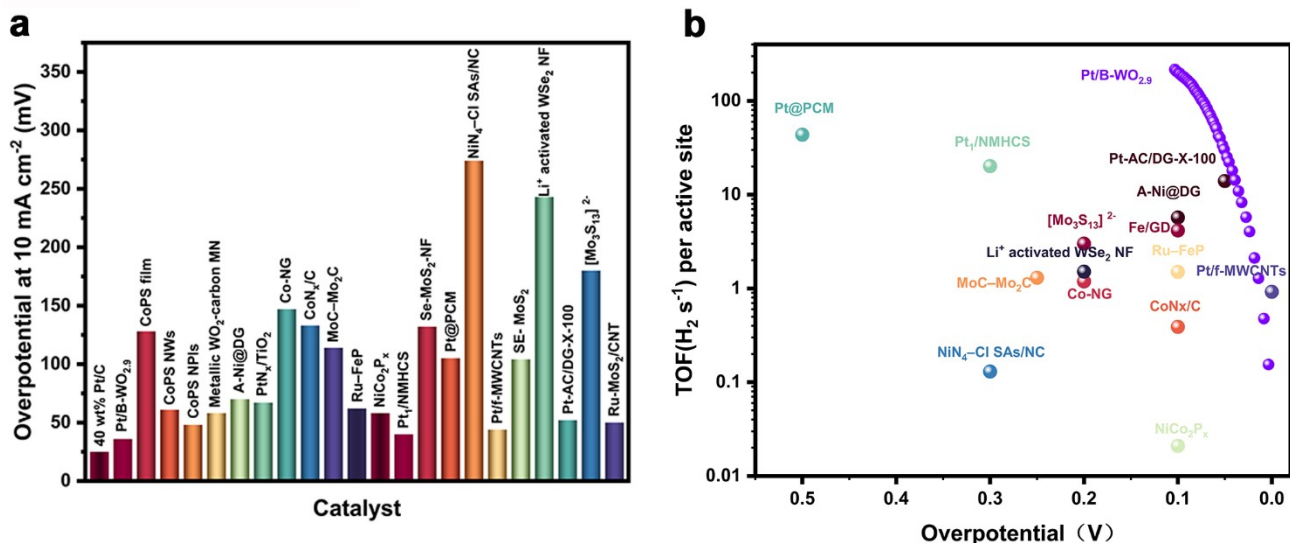


**Figure S10.** Comparison of the overpotential and TOF with other catalysts. (a) Overpotentials of Pt/B-WO<sub>2.9</sub> and other reported electrocatalysts at 10 mA cm<sup>-2</sup> in acidic electrolytes (**Table S3**). (b) TOF of Pt/B-WO<sub>2.9</sub> and other reported electrocatalysts in acidic electrolytes (**Note S2**).

**Note S1:** Algorithm of TOF

Number of gases generated per second (H<sub>2</sub>):

$$\begin{aligned} \# \text{ Hydrogen} &= (j \text{ cm}^2) \left( \frac{1 \text{ C s}^{-1}}{1000 \text{ mA}} \right) \left( \frac{1 \text{ mol e}^{-1}}{96485.3 \text{ C}} \right) \left( \frac{1 \text{ mol H}_2}{2 \text{ mol e}^{-1}} \right) \left( \frac{6.022 * 10^{23} \text{ H}_2 \text{ molecules}}{1 \text{ mol H}_2} \right) \\ &= 3.12 * 10^{15} * /j/ \text{ H}_2 \text{ molecules per second} \end{aligned}$$

M(Pt)=195.1g/mol.

The amount of Pt measured by ICP is 0.00086mg (**Table S3**) per carbon paper (1x1 cm<sup>2</sup>). The amount of B-WO<sub>2.9</sub> is 0.5mg per carbon paper (1x1 cm<sup>2</sup>).

$$n(\text{Pt}) = 0.00086\text{mg}/(195.1\text{g/mol}) = 4.41 * 10^{-6} \text{mmol} = 4.41 * 10^{-9} \text{mol}$$

The total number of active sites in the catalyst (Pt):

$$\# \text{ Catalyst (Pt)} = n(\text{Pt}) * N_A = 4.41 * 10^{-9} \text{mol} * 6.022 * 10^{23} \text{ mol}^{-1} = 26.6 * 10^{14}$$

$$\text{TOF} = \frac{\# \text{ gas} * /j/}{\# \text{ catalyst}}$$

$$\text{TOF} = \frac{3.12 * 10^{15} * /j/ \text{ H}_2 \text{ molecules per second}}{26.6 * 10^{14} \text{ per active site}} = 1.17 * /j/ \text{ H}_2 \text{ s}^{-1} \text{ per active site}$$

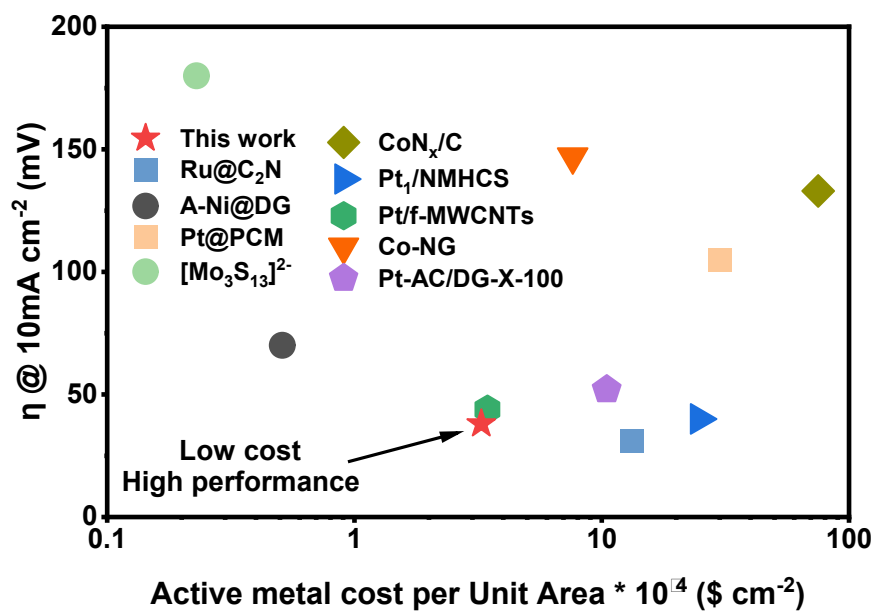


**Figure S11.** Comparison of the cost-effectiveness and catalytic performance of Pt/B-WO<sub>2.9</sub> with other reported HER catalysts. The plot illustrates the relationship between the active metal cost per unit area and the overpotential at 10 mA cm<sup>-2</sup> for Pt/B-WO<sub>2.9</sub> and various reported electrocatalysts (Table S4).

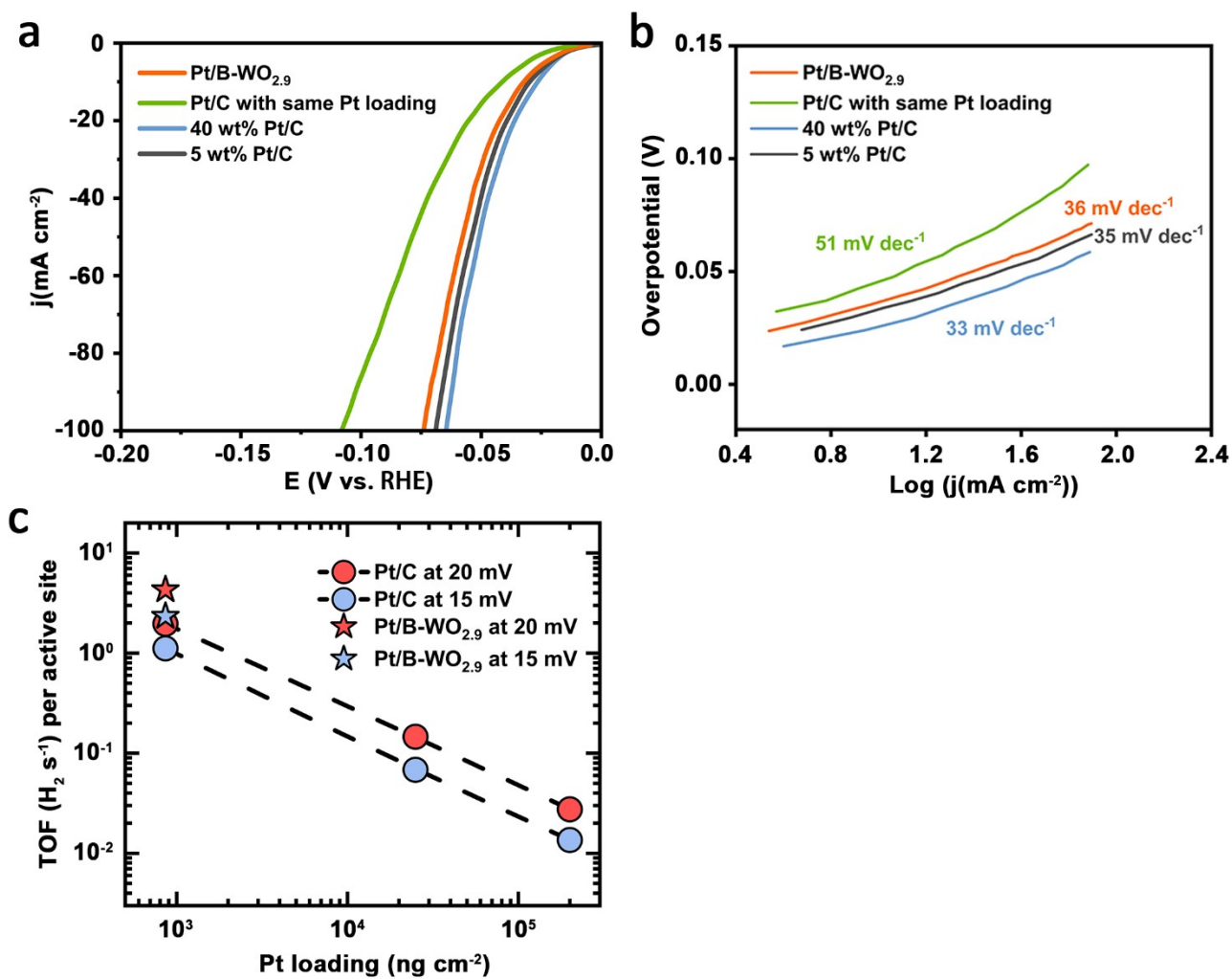


**Figure S12.** Electrochemical performance of catalysts with different Pt loading. (a) LSV curves of Pt/B-WO<sub>2.9</sub> and different Pt loading samples in 0.5 M H<sub>2</sub>SO<sub>4</sub>. (b) Tafel slopes of the samples. (c) TOF at  $\eta = 15$  mV and 20 mV vs. Pt loading for Pt/B-WO<sub>2.9</sub> and different Pt loading samples.

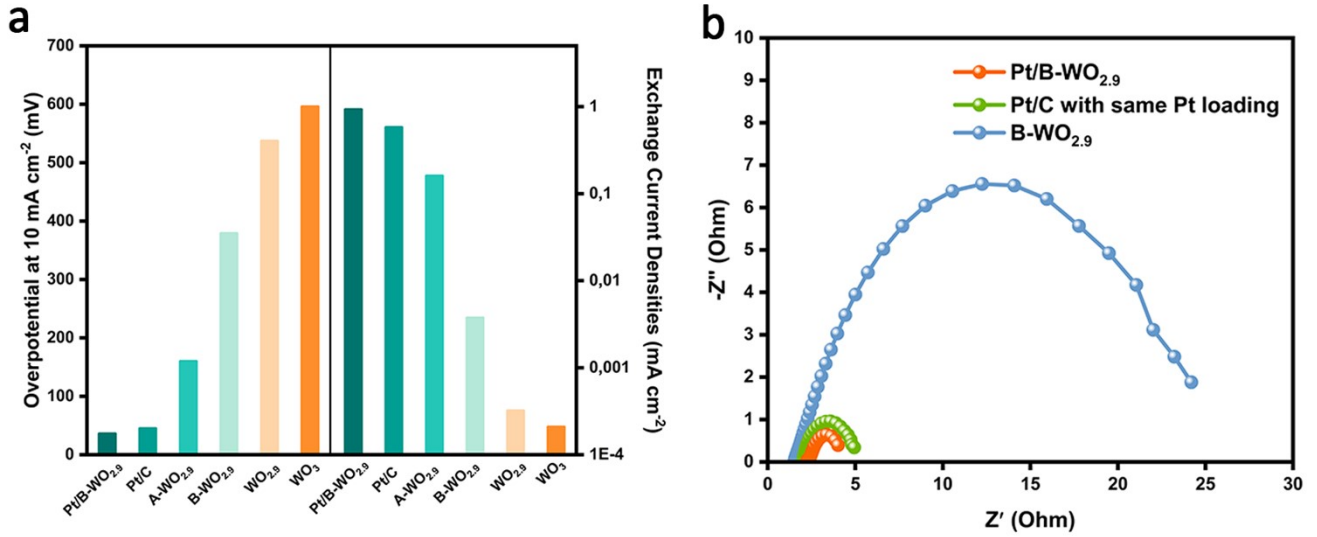


**Figure S13.** Electrochemical performance. (a) Overpotentials at 10 mA cm<sup>-2</sup> (left) and exchange current densities (right) of Pt/C (40 wt%), Pt/B-WO<sub>2.9</sub>, A-WO<sub>2.9</sub>, B-WO<sub>2.9</sub>, WO<sub>2.9</sub> and WO<sub>3</sub> (**Note S3**). (b) EIS Nyquist plots of Pt/B-WO<sub>2.9</sub>, Pt/C with same Pt loading and B-WO<sub>2.9</sub>. The charge transfer resistance (R<sub>ct</sub>) of Pt/B-WO<sub>2.9</sub> is 2.1 Ω, Pt/C with same Pt loading as Pt/B-WO<sub>2.9</sub> is 2.9 Ω, B-WO<sub>2.9</sub> is 24.3Ω.

**Note S2:** Algorithm of Exchange Current Densities

Derived from the Butler-Volmer equation

$$\eta = \frac{2.303 R T}{\alpha F} * \log (j_0) - \frac{2.303 R T}{\alpha F} * \log(j)$$

It can be known that  $\eta$  is a function of  $\log (j)$ , the intercept of the function is

$$\frac{2.303 R T}{\alpha F} * \log (j_0), \text{ and the slope is } -\frac{2.303 R T}{\alpha F}.$$

Therefore, it can be obtained :

$$\log (j_0) = -\frac{\text{intercept}}{\text{slope}}$$

$$j_0 = 10^{\left(-\frac{\text{intercept}}{\text{slope}}\right)}$$

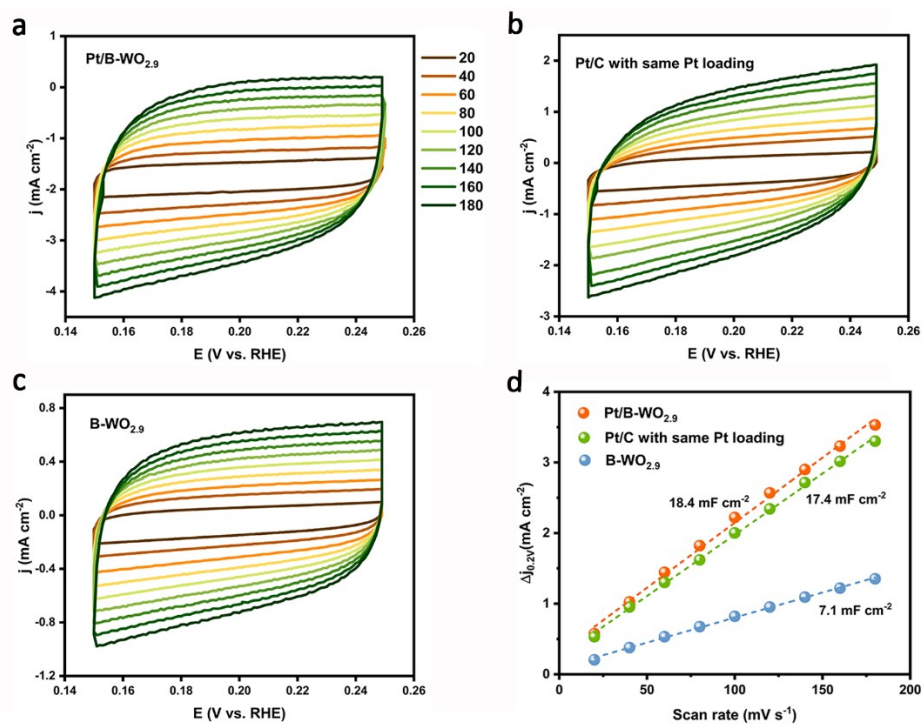


**Figure S14.**  $C_{dl}$  measurement. CV curves of (a) Pt/B-WO<sub>2.9</sub>, (b) Pt/C with same Pt loading and (c) B-WO<sub>2.9</sub> collected in the non-faradic current range at scan rates of 20, 40, 60, 80, 100, 120, 140, 160 and 180 mV s<sup>-1</sup> in 0.5 M H<sub>2</sub>SO<sub>4</sub> electrolyte. (d) Corresponding calculated  $C_{dl}$  value of Pt/B-WO<sub>2.9</sub> is 18.4 mF cm<sup>-2</sup>, Pt/C with same Pt loading is 17.4 mF cm<sup>-2</sup> and B-WO<sub>2.9</sub> is 7.1 mF cm<sup>-2</sup>.

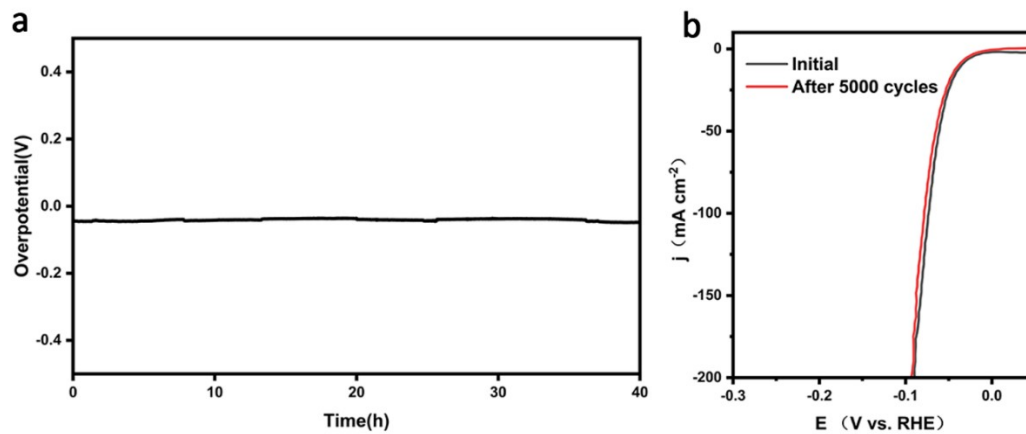


**Figure S15.** (a) Stability tests (Chronopotentiometry test) at 10 mA cm<sup>-2</sup>. (b) Polarization curves of Pt/B-WO<sub>2.9</sub> before and after 5000 CV cycles.

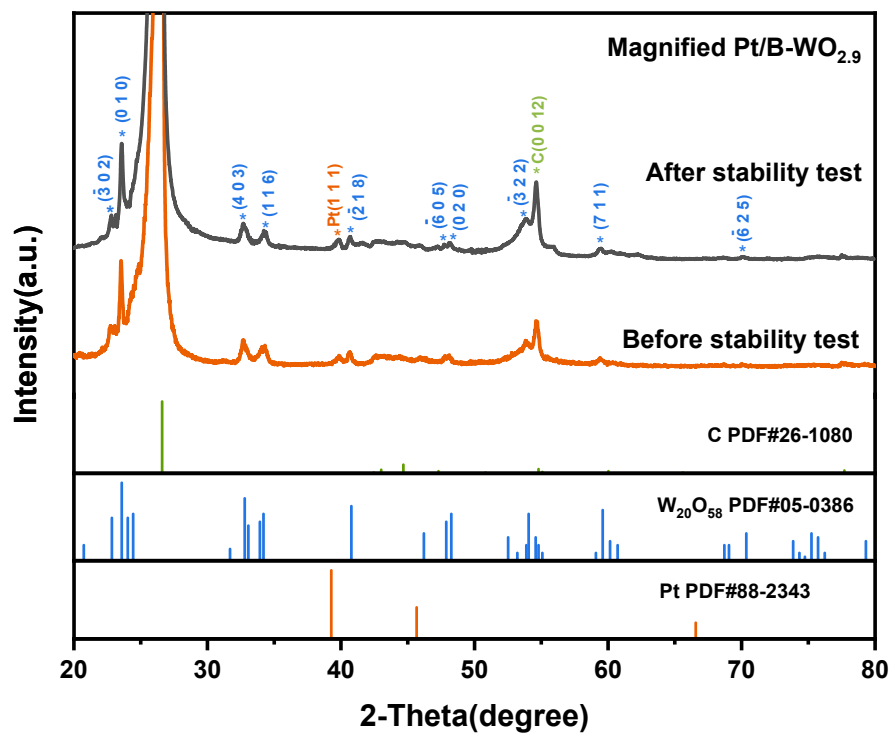


**Figure S16.** XRD patterns of Pt/B-WO<sub>2.9</sub> before and after the stability test.

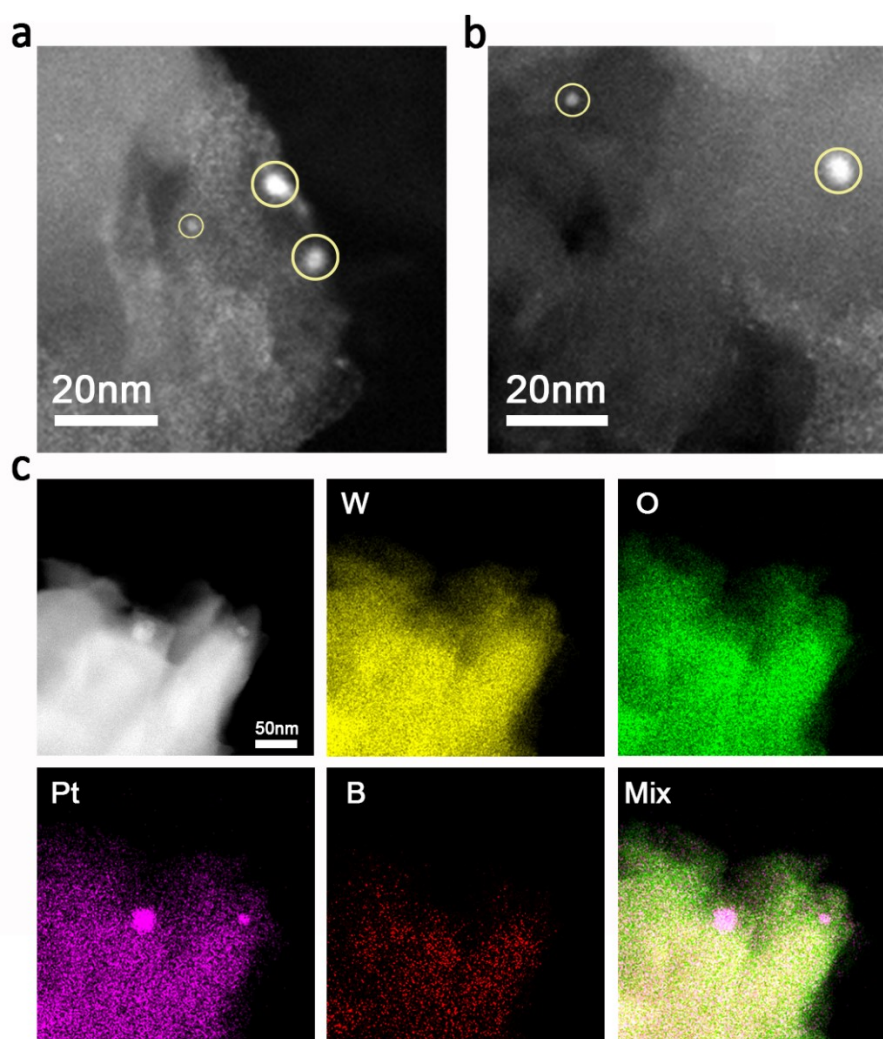


**Figure S17.** Morphology of the Pt/B-WO<sub>2.9</sub> after electrochemical stability test. (a-b) HAADF-STEM images of Pt/B-WO<sub>2.9</sub> after electrochemical stability test, Pt is surrounded by yellow circles. (c) EDS elemental mapping images of Pt/B-WO<sub>2.9</sub> after electrochemical stability test.

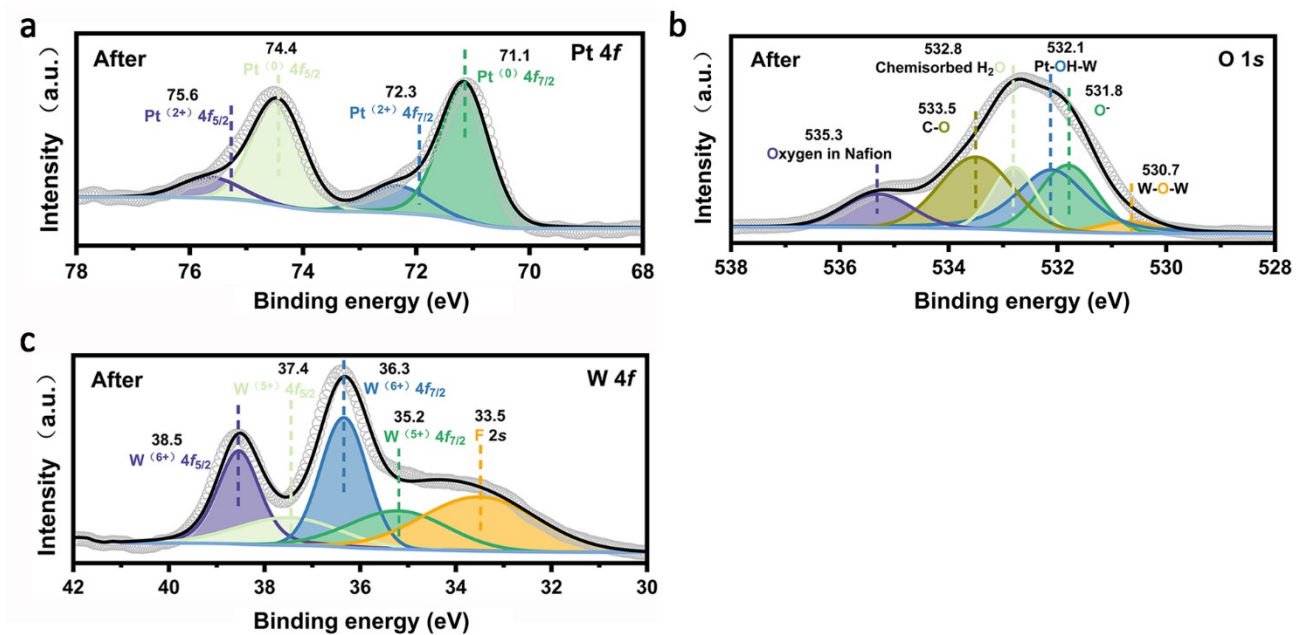


**Figure S18.** XPS spectra of Pt/B-WO<sub>2.9</sub> after electrochemical stability test. (a) W 4f spectra. (b) O 1s spectra. (c) Pt 4f spectra.

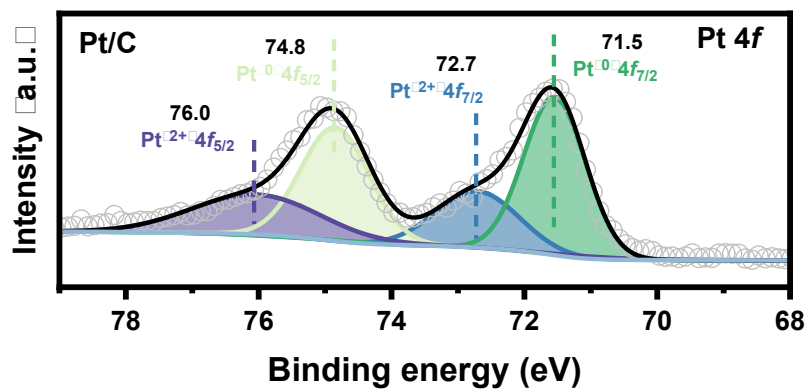
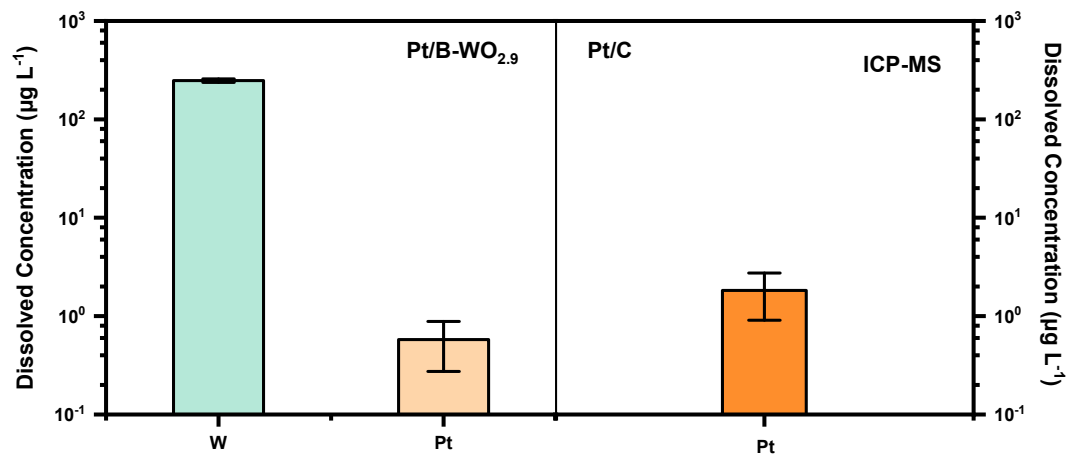
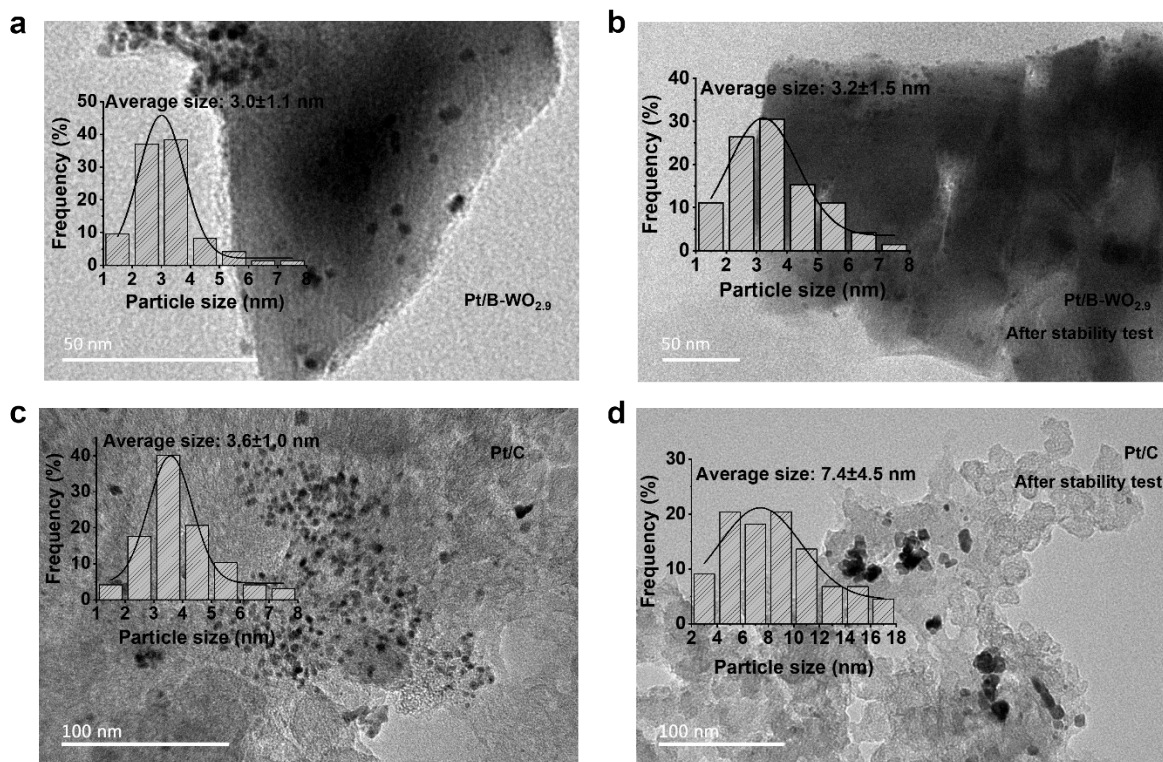


Figure S19. XPS spectra of Pt 4f of Pt/C.



**Figure S20.** Comparison of the dissolved metal concentrations of Pt/B-WO<sub>2.9</sub> and Pt/C after stability tests.



**Figure S21.** TEM images and particle size distribution histograms of Pt/B-WO<sub>2.9</sub> and Pt/C before and after stability test. Pt/B-WO<sub>2.9</sub> before (a) and after (b) stability test. Pt/C before (c) and after (d) stability test. The insets show the corresponding particle size distributions with average sizes labeled.

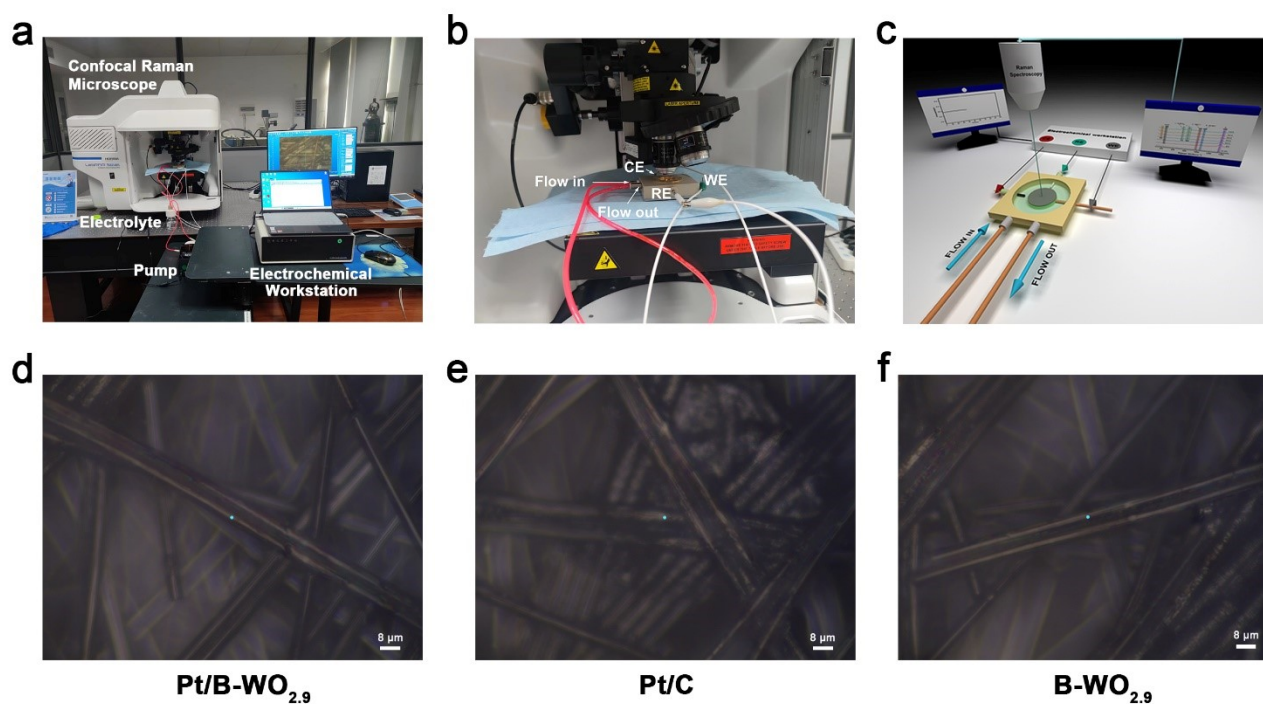


**Figure S22.** Schematic of the in situ Raman experiment and optical image of the region detected by the in-situ Raman excitation laser. (a,b) The set-up of the in-situ Raman measurements. (c) Schematic of the Raman experimental set-up. (d) Pt/B-WO<sub>2.9</sub> on carbon paper. (e) Pt/C with same Pt loading on carbon paper. (f) B-WO<sub>2.9</sub> on carbon paper.

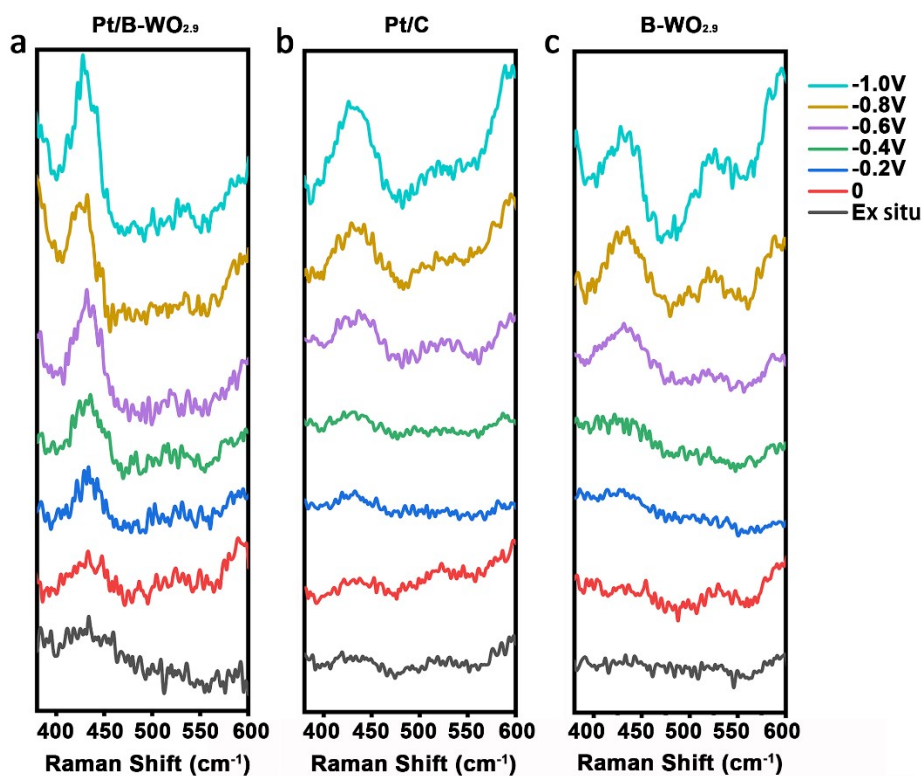


**Figure S23.** In situ Raman spectra. (a) Pt/B-WO<sub>2.9</sub>. (b) Pt/C with same Pt loading and (c) B-WO<sub>2.9</sub> in 0.5 M H<sub>2</sub>SO<sub>4</sub> saturated with H<sub>2</sub>. The peak around 425 cm<sup>-1</sup> can be assigned to the vibrational peak of liquid water with ordered structure. Ordered interfacial water ‘H-down’ means that when the electrode is negatively charged, the average orientation of hydrogen in the interfacial water molecules is toward the electrode, in contrast, oxygen is directed away from the electrode<sup>9</sup>.

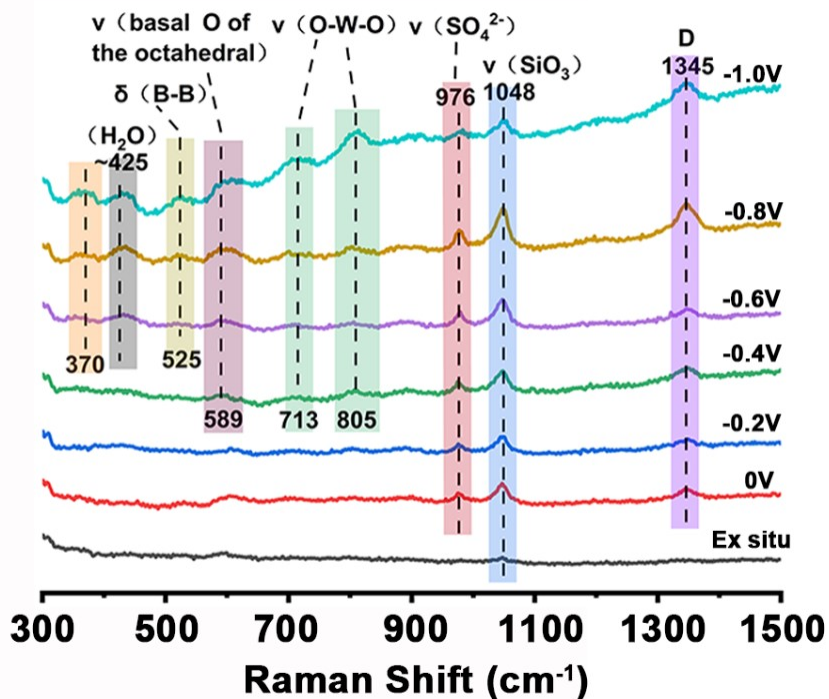


**Figure S24.** In situ Raman spectra of B-WO<sub>2.9</sub> in 0.5 M H<sub>2</sub>SO<sub>4</sub>/H<sub>2</sub>O saturated with H<sub>2</sub>.

**Note S3:** The attribution of Raman peak

The  $\nu(\text{O-W-O})$  at 713 and 805  $\text{cm}^{-1}$  became obvious when the applied voltage reached -0.4 V, indicating that with the gradual decrease of the bias voltage, the originally symmetrical WO<sub>6</sub> octahedron gradually deviates from the cubic phase WO<sub>3</sub> structure<sup>10</sup>. The peak at 370  $\text{cm}^{-1}$ , which is similar to the variation trend of  $\nu(\text{O-W-O})$ , can be regarded as the peak of phonon density of states<sup>11</sup>. And 976  $\text{cm}^{-1}$  is assigned to the  $\nu_1(\text{SO}_4)^{2-}$  symmetric stretching mode from electrolyte<sup>12</sup>. 1048  $\text{cm}^{-1}$  is attributed to the symmetric stretching vibrations modes of  $\nu_1\text{-SiO}_3$  from the quartz glass on Raman cell<sup>13</sup>. 1345  $\text{cm}^{-1}$  is the D peak of carbon paper<sup>14</sup>. The peak at 525  $\text{cm}^{-1}$  is attributed to the  $\delta(\text{B-B})$  bending vibration<sup>15</sup>. The peak at 589  $\text{cm}^{-1}$  is the symmetric stretching mode of the basal oxygens on the WO<sub>6</sub> octahedral, while Pt/B-WO<sub>2.9</sub> does not have, indicating that the basal oxygen on the WO<sub>6</sub> octahedron of Pt/B-WO<sub>2.9</sub> is asymmetric<sup>16</sup>.

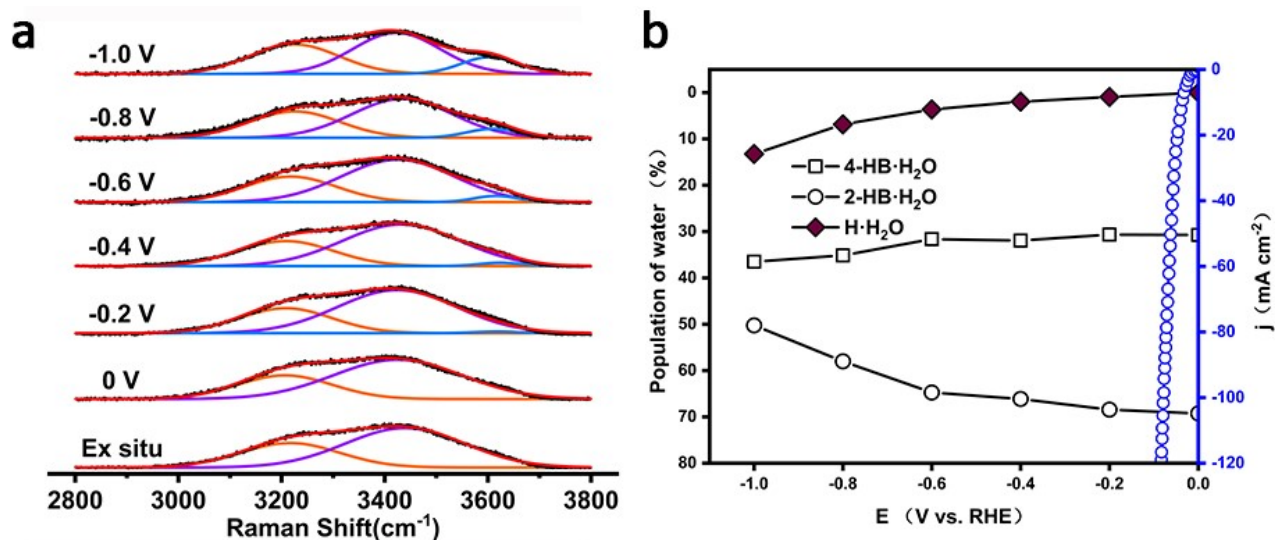


**Figure S25.** In situ Raman spectra of Pt/B-WO<sub>2.9</sub>. (a) Gaussian fits for the three O-H stretching modes are shown in orange (4-HB·H<sub>2</sub>O), purple (2-HB·H<sub>2</sub>O), and blue (H·H<sub>2</sub>O), respectively. (b) Potential-dependent population of interfacial water was obtained by integrating the corresponding vibration modes in (a), and HER current density was recorded in a three-electrode electrochemical cell.

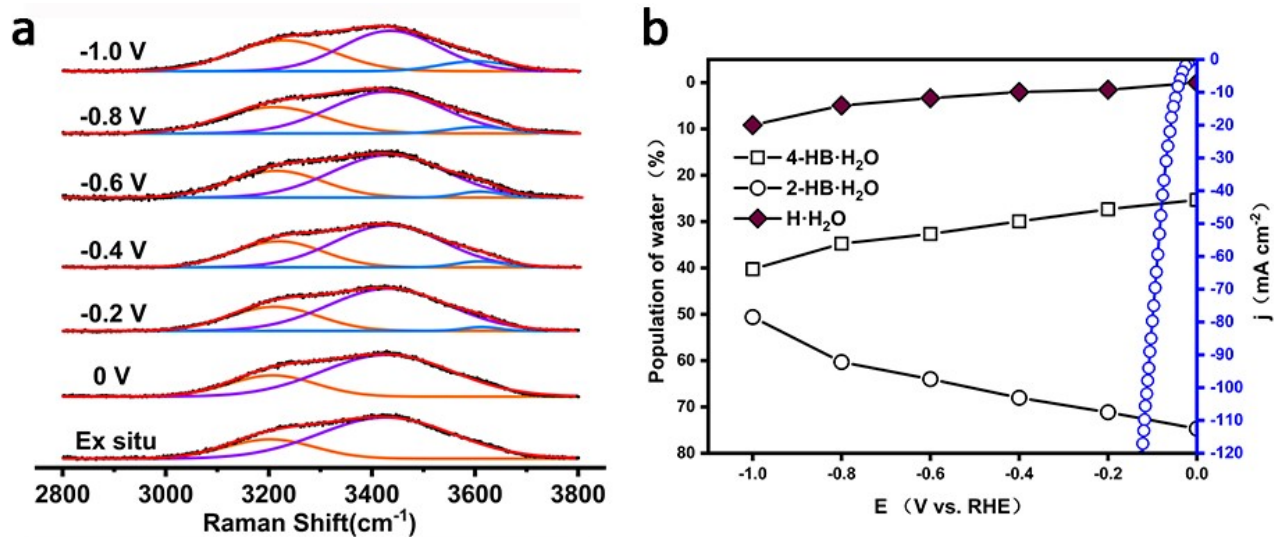


**Figure S26.** In situ Raman spectra of Pt/C with same Pt loading as Pt/B-WO<sub>2.9</sub>. (a) Gaussian fits for the three O-H stretching modes are shown in orange (4-HB·H<sub>2</sub>O), purple (2-HB·H<sub>2</sub>O), and blue (H·H<sub>2</sub>O), respectively. (b) Potential-dependent population of interfacial water was obtained by integrating the corresponding vibration modes in (a), and HER current density was recorded in a three-electrode electrochemical cell.

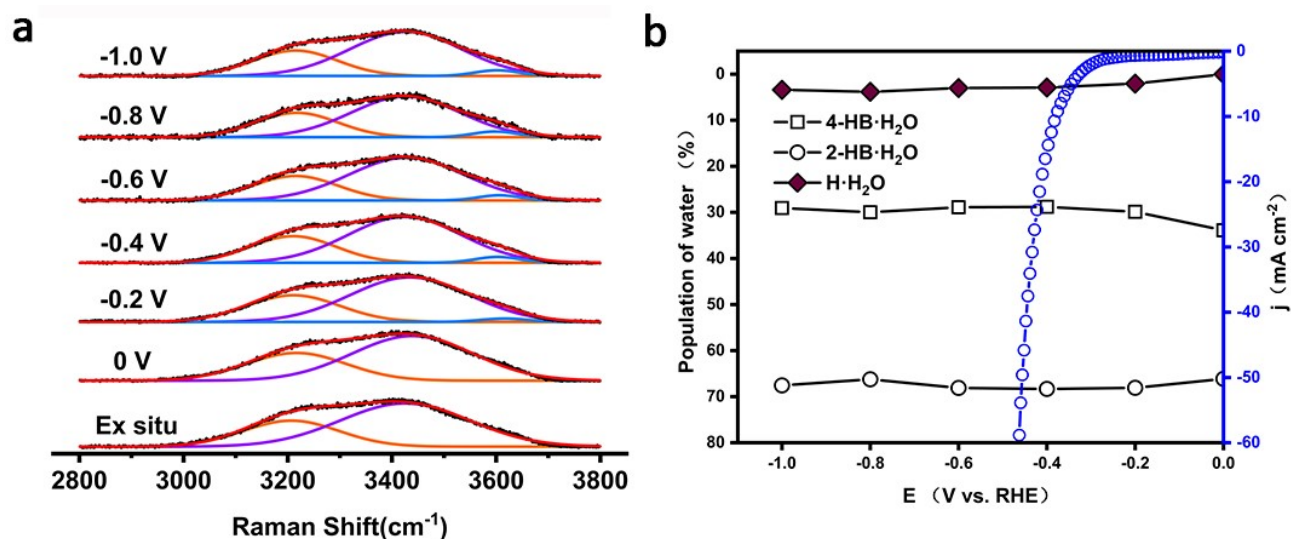


**Figure S27.** In situ Raman spectra of B-WO<sub>2.9</sub>. (a) Gaussian fits for the three O-H stretching modes are shown in orange (4-HB·H<sub>2</sub>O), purple (2-HB·H<sub>2</sub>O), and blue (H·H<sub>2</sub>O), respectively. (b) Potential-dependent population of interfacial water was obtained by integrating the corresponding vibration modes in (a), and HER current density was recorded in a three-electrode electrochemical cell.

**Note S4:** Deuterium isotope substitution experiment in the Raman spectroscopy

In order to verify whether the peak around 2023 cm<sup>-1</sup> in the Raman spectrum corresponds to the Pt-H vibration mode, we recorded the in-situ Raman results of Pt/B-WO<sub>2.9</sub> in 0.5 M D<sub>2</sub>SO<sub>4</sub>/D<sub>2</sub>O saturated with N<sub>2</sub>. The corresponding Raman frequency downward shift ratio ( $\gamma$ ) in the isotope experiment is:

$$\gamma = \nu(PtD)/\nu(PtH) = \frac{\sqrt{m(Pt) + m(D)}}{\sqrt{m(Pt) \times m(D)}} \div \frac{\sqrt{m(Pt) + m(H)}}{\sqrt{m(Pt) \times m(H)}} = \frac{\sqrt{195.1 + 2}}{\sqrt{195.1 \times 2}} \div \frac{\sqrt{195.1 + 1}}{\sqrt{195.1 \times 1}} =$$

70.89%

Therefore, in the isotope experiment, the Raman peak near 2023 cm<sup>-1</sup> should be shifted to 2023 × 70.89% = 1434 cm<sup>-1</sup>, which is close to the observed value of 1428 cm<sup>-1</sup>, so the peak near 2023 cm<sup>-1</sup> can be attributed to the Pt-H vibration.

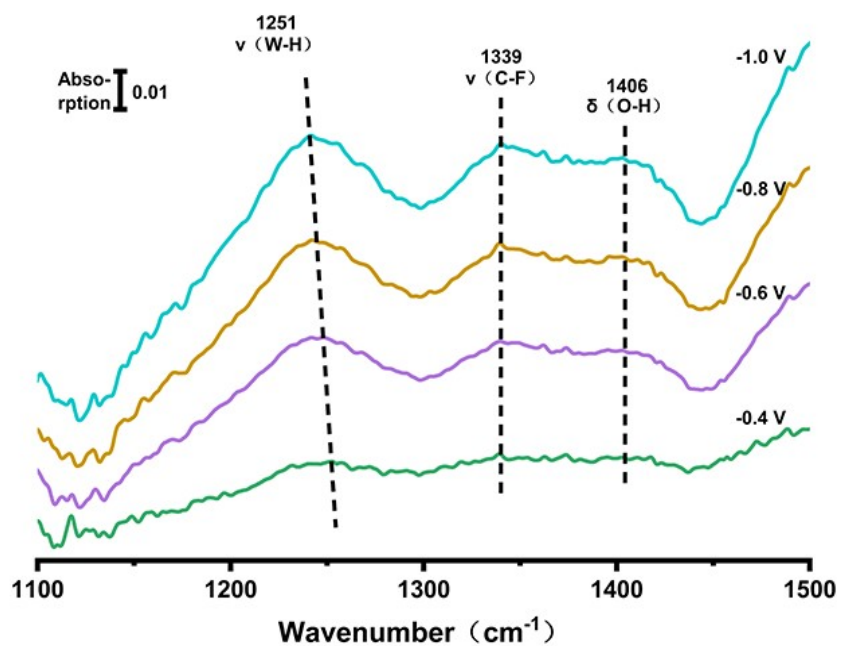


**Figure S28.** In situ ATR-SEIRAS spectroscopy of Pt/B-WO<sub>2.9</sub>. Magnified spectroscopy of Pt/B-WO<sub>2.9</sub> in 0.5 M H<sub>2</sub>SO<sub>4</sub>. The band centred at 1339 cm<sup>-1</sup> can be assigned to ν(C-F) stretch vibrations from Nafion<sup>17</sup>. The band centred at 1406 cm<sup>-1</sup> can be attributed to δ(O-H) bending vibrations from H<sub>2</sub>O<sup>18</sup>.

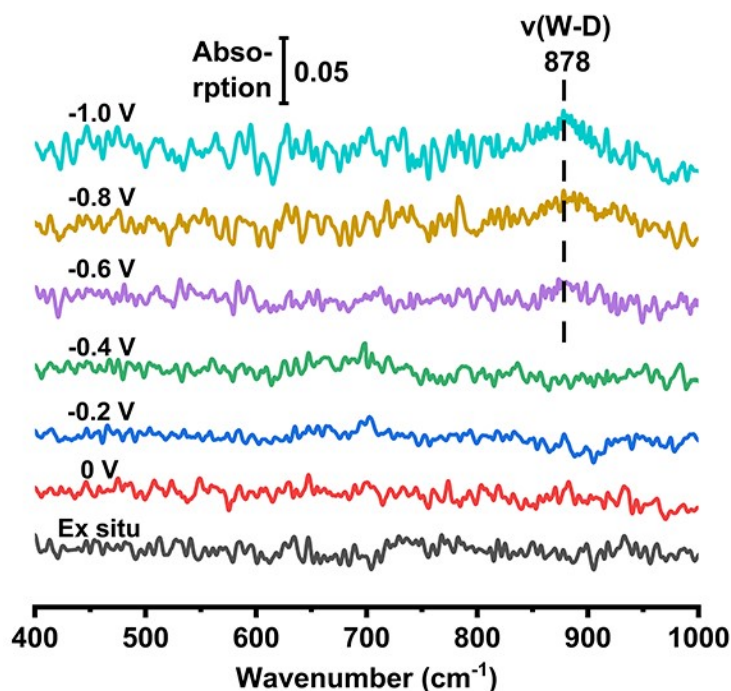


**Figure S29.** In situ ATR-SEIRAS spectroscopy of Pt/B-WO<sub>2.9</sub> in 0.5 M D<sub>2</sub>SO<sub>4</sub>/D<sub>2</sub>O saturated with N<sub>2</sub>.

**Note S5:** Deuterium isotope substitution experiment in the ATR-SEIRAS spectroscopy

In order to verify whether the peak around 1241 cm<sup>-1</sup> in the ATR-SEIRAS spectrum corresponds to the W-H vibration mode, we recorded the in situ ATR-SEIRAS results of Pt/B-WO<sub>2.9</sub> in 0.5 M D<sub>2</sub>SO<sub>4</sub>/D<sub>2</sub>O saturated with N<sub>2</sub>. The corresponding wavenumber downward shift ratio ( $\gamma$ ) in the isotope experiment is:

$$\gamma = \nu(WD)/\nu(WH) = \frac{\sqrt{m(W) + m(D)}}{\sqrt{m(W) \times m(D)}} \div \frac{\sqrt{m(W) + m(H)}}{\sqrt{m(W) \times m(H)}} = \frac{\sqrt{183.9 + 2}}{\sqrt{183.9 \times 2}} \div \frac{\sqrt{183.9 + 1}}{\sqrt{183.9 \times 1}} = 0.7090$$

0.90%

Therefore, in the isotope experiment, the peak near 1241 cm<sup>-1</sup> should be shifted to 1241 × 0.7090 = 880 cm<sup>-1</sup>, which is close to the observed value of 878 cm<sup>-1</sup>, so the peak near 1241 cm<sup>-1</sup> can be attributed to the W-H vibration.

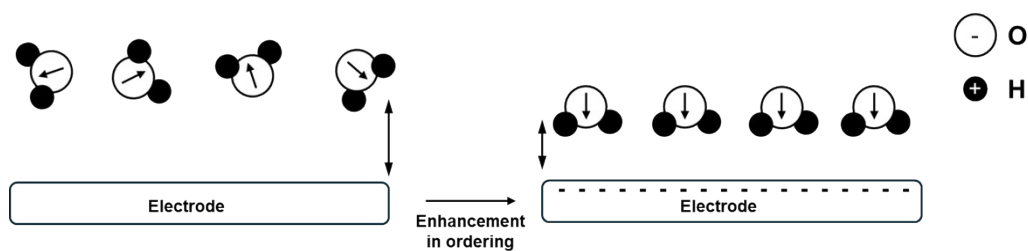


**Figure S30.** Influence of Electrode Polarization on Interfacial Water Structure. This diagram illustrates the effect of electrode polarization on the orientation of interfacial water molecules. On the left side, under a small negative bias ( $V_0$ ), water molecules exhibit a random orientation, forming a disordered hydrogen-bond network. On the right side, under a large negative bias ( $V_1$ ), the accumulation of negative charge on the electrode surface induces a reorientation of water molecules, aligning their hydrogen atoms toward the electrode, forming the characteristic "two-H-down" configuration.

**Note S6:** Calculation of conventional kinetic model

If the noble metals only lead to the change of the electronic structure on the B-WO<sub>2.9</sub>, thereby enhancing the kinetic process of HER, the kinetic model can be divided into the following four situations<sup>19</sup>, 1) Volmer-Tafel mechanism (Volmer as rate determining step (RDS)); 2) Volmer-Tafel mechanism (Tafel as RDS); 3) Volmer-Heyrovsky mechanism (Volmer as RDS); and 4) Volmer-Heyrovsky mechanism (Heyrovsky as RDS). Where the primitive reaction is shown below:



--Tafel step



step

If follow the Volmer-Tafel mechanism

1) If Volmer is the RDS,  $\theta_{\text{Pt-H}}$  is close to zero, and the net rate of hydrogen production can be written as:

$$r = k_1 a_{\text{H}_3^+ \text{O}} (1 - \theta_{\text{Pt-H}}) = k_1 a_{\text{H}_3^+ \text{O}}$$

where  $k$  is the reaction rate constant,  $\theta$  is the percentage of active sites covered by H, and  $a_{\text{H}_3^+ \text{O}}$  is the activity of hydronium ions.

Furthermore, by deriving the Butler-Volmer equation:

$$j = j_0 \exp(-\alpha \eta F/RT) - j_0 \exp[-(1-\alpha) \eta F/RT]$$

we can get the following formula<sup>20</sup>:

$$k_i = k_{i0} \exp(-\alpha F \eta / RT)$$

$$k_{-i} = k_{-i0} \exp((1-\alpha) F \eta / RT)$$

$$r = k_1 a_{\text{H}_3^+ \text{O}} = k_{10} a_{\text{H}_3^+ \text{O}} e^{-\frac{\alpha F \eta}{RT}},$$

$$-j = Fr$$

$$\log_{10}(-j) = \text{const} + \log_{10}(a_{\text{H}_3^+ \text{O}}) - \frac{\alpha F \eta}{2.303 RT}$$

The measured slope of  $\log_{10}(-j)$  as a function of pH ( $-\log_{10}(a_{\text{H}_3^+ \text{O}})$ ) is -1.16, which is very close to our kinetic calculation of -1.

Faraday's constant,  $F = 96500 \text{ C mol}^{-1}$ ; the gas constant,  $R = 8.314 \text{ J mol}^{-1} \text{ K}^{-1}$ ; the absolute temperature,  $T = 293.15 \text{ K}$ .

However, to solve for the Tafel slope, we still have a parameter  $\alpha$  that is unknown, so now we will go to solve for  $\alpha$ .

At potential  $E$ , as shown in Figure S31, the activation energy of the forward reaction is:

$$\Delta G_f^\ddagger + (1-\alpha)F(E-E^{0'}) = \Delta G_{0f}^\ddagger + F(E-E^{0'})$$

$$\text{So: } \Delta G_f^\ddagger = \Delta G_{0f}^\ddagger + \alpha F(E-E^{0'})$$

Among them,  $E^{0'}$  is the initial potential,  $E$  is the half cell potential,  $\Delta G_{0f}^\ddagger$  is the activation free energy of the positive reaction at the initial potential, and  $\Delta G_f^\ddagger$  is the activation free energy of the positive reaction at the half cell potential<sup>21</sup>.

$$\alpha = F \frac{\partial \Delta G_f^\ddagger}{\partial E}$$

It can be deduced that:

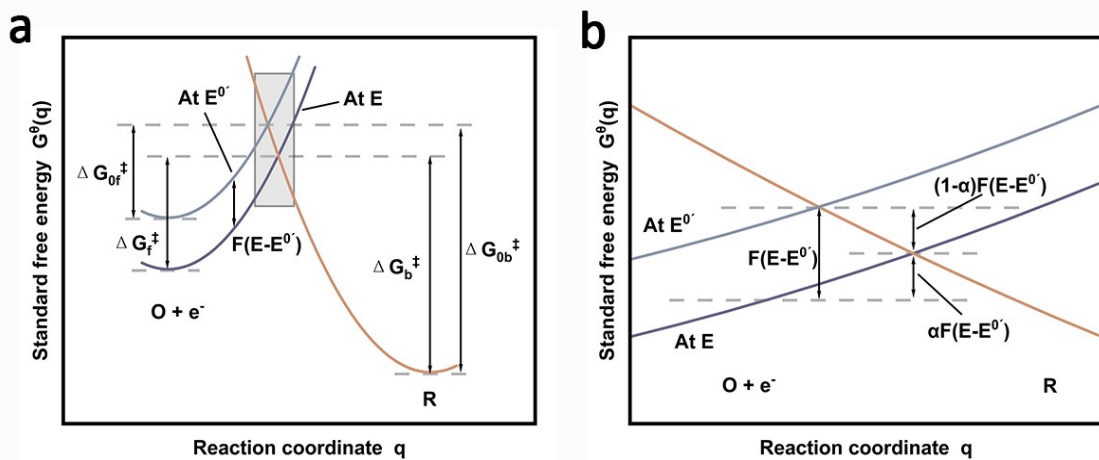
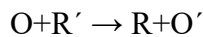


**Figure S31.** The relationship between the standard Gibbs free energy and the reaction coordinates. (a) Influence of external bias on the standard activation energy of oxidizing and reducing species. (b) magnified region in (a) rectangle.

In addition, since the proton has only electrostatic interaction with the electrode surface without specific adsorption, and the cation has a high degree of hydration, it can be regarded as an outer sphere reaction, and electrons are transferred from the electrode to the substance  $O$  to form the product  $R$ . This process associates the reduction of  $O$  to  $R$  with an appropriate reducing agent  $R'$ :



According to the two general assumptions of the Marcus theory (1) the reactant  $O$  is concentrated at a fixed position away from the electrode; (2) the standard free energies,  $G_O$  and  $G_R$ , of reactant  $O$  and product  $R$ , are both squared with the reaction coordinates<sup>22</sup>:

$$G_O(q) = \left(\frac{k}{2}\right) * (q - q_O)^2$$

$$G_R(q) = \left(\frac{k}{2}\right) * (q - q_R)^2 + \Delta G^0$$

Here,  $q$  is the reaction coordinate,  $q_O$  and  $q_R$  are the coordinate values relative to the equilibrium atomic configuration of O and R;  $k$  is a proportional constant;  $\Delta G^0$  is the reaction free energy of electron transfer.

According to the Frank-Condon principle, electrons can only effectively transition between two particles with close electron energy levels, and due to the large mass difference between atoms and electrons, atoms can be considered static when electron transfer occurs. Therefore, the transition state should have the same configuration position on the O and R curve, which is represented by  $q^\ddagger$  on the reaction coordinate (Figure S25). That is, the relationship  $G_O(q^\ddagger) = G_R(q^\ddagger)$  should be satisfied, and the free energy of the transition state is as follows:

$$G_O(q^\ddagger) = \left(\frac{k}{2}\right) * (q^\ddagger - q_O)^2$$

$$G_R(q^\ddagger) = \left(\frac{k}{2}\right) * (q^\ddagger - q_R)^2 + \Delta G^0$$

$$\text{The solutions should be: } q^\ddagger = \frac{q_R + q_O}{2} + \frac{\Delta G^0}{k(q_R - q_O)}$$

$$\text{because of: } \Delta G_f^\ddagger = G_O(q^\ddagger) - G_O(q_O) = G_O(q^\ddagger)$$

$$\Delta G_f^\ddagger \text{ can be written as: } \Delta G_f^\ddagger = \frac{k(q_R - q_O)^2}{8} \left[1 + \frac{2\Delta G^0}{k(q_R - q_O)^2}\right]^2$$

$$\text{Define reorganization energy } \lambda = \left(\frac{k}{2}\right) * (q_R - q_O)^2, \text{ so } \Delta G_f^\ddagger = \frac{\lambda}{4} \left[1 + \frac{\Delta G^0}{\lambda}\right]^2$$

$$\text{because of: } \Delta G^0 = F(E - E^0)$$

$$\Delta G_f^\ddagger \text{ can be written as: } \Delta G_f^\ddagger = \frac{\lambda}{4} \left[1 + \frac{F(E - E^0)}{\lambda}\right]^2$$

Here,  $E$  is the half cell potential,  $E^0$  is the "standard" half cell potential in the commonly used medium.

After getting the functional relationship between  $\Delta G_f^\ddagger$  and  $E$ , we can start solving for  $\alpha$ :

$$\alpha = \frac{1}{F} \frac{\partial \Delta G_f^\ddagger}{\partial E} = \frac{1}{2} \left[1 + \frac{F(E - E^0)}{\lambda}\right]$$

Since the hydrogen production rate  $r$  obtained earlier is assumed at low overpotential, the second term  $(F(E - E^0))/\lambda$  can be approximated to 0 (Or see it as  $\Delta G^0/\lambda$  in Supplementary Fig. 32), so  $\alpha \approx 0.5$ , and now we can solve for the Tafel slope.

$$\text{Tafel slope} = \frac{2.303RT}{\alpha F} \approx 116 \text{ mV/dec, which is far from the experimental value of 33 mV/dec.}$$

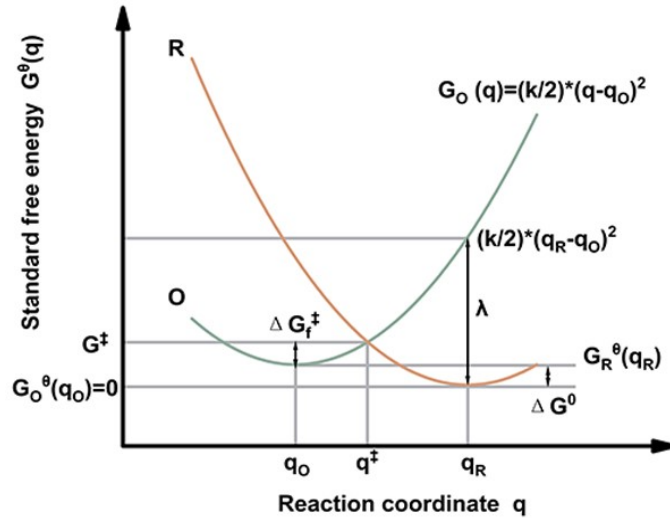


**Figure S32.** The standard Gibbs free energy of electron transfer reactions between oxidizing and reducing species as a function of reaction coordinates

2) If Tafel is the RDS, Volmer step will be equilibrated ( $r_1 = r_{-1}$ ), the net rate of hydrogen production can be written as:

$$r = k_2 \theta_{Pt-H} \theta_{Pt-H};$$

$$r_1 = k_1 a_{H_3^+O} (1 - \theta_{Pt-H}); r_{-1} = k_{-1} \theta_{Pt-H};$$

$$\theta_{Pt-H} = \frac{\frac{a_{H_3^+O}}{k_{-1}}}{\frac{a_{H_3^+O}}{k_1} + \frac{k_{-10}}{k_1} e^{\frac{F\eta}{RT}}} = \frac{a_{H_3^+O}}{a_{H_3^+O} + \frac{k_{-10}}{k_1} e^{\frac{F\eta}{RT}}}$$

Since Tafel step does not involve electron transfer, so  $k_2 = k_{20}$ , and at low overpotential, we can get the following approximation:

$$r = k_2 \theta_{Pt-H} \theta_{Pt-H} = k_{20} \left( \frac{a_{H_3^+O}}{a_{H_3^+O} + \frac{k_{-10}}{k_1} e^{\frac{F\eta}{RT}}} \right)^2$$

$$= k_{20} * a_{H_3^+O}^2 / (a_{H_3^+O}^2 + 2a_{H_3^+O} * \frac{k_{-10}}{k_{10}} * \exp\left(\frac{F\eta}{RT}\right) + \left(\frac{k_{-10}}{k_{10}}\right)^2 * \exp\left(\frac{2F\eta}{RT}\right)) \approx k_{20} * a_{H_3^+O}^2 * \left(\frac{k_{-10}}{k_{10}}\right)^{-2} * \exp\left(-\frac{2F\eta}{RT}\right)$$

$$\log_{10}(-j) = \text{const} + 2 \log_{10}(a_{H_3^+O}) - \frac{2F\eta}{2.303RT}$$

The calculated slope of  $\log_{10}(-j)$  as a function of pH ( $-\log_{10}(a_{H_3^+O})$ ) is -2, which is not close to the measured value -1.16.

If follow the Volmer-Heyrovsky mechanism

3) If Volmer is the RDS, the net rate of hydrogen production is the same as the rate of Volmer as RDS in the Volmer-Tafel mechanism,  $\theta_{Pt-H}$  is close to zero.

$$r = k_1 a_{H_3^+O} (1 - \theta_{Pt-H}) = k_1 a_{H_3^+O} = k_{10} a_{H_3^+O} e^{-\frac{\alpha F\eta}{RT}}$$

$$\log_{10}(-j) = \text{const} + \log_{10}(a_{H_3^+O}) - \frac{\alpha F\eta}{2.303RT}$$

Tafel slope  $\frac{2.303RT}{\alpha F} \approx 116$  mV/dec, not consistent with the experimental value of 33 mV/dec.

4) If Heyrovsky is the RDS, Volmer step will be equilibrated ( $r_1 = r_{-1}$ ), we can get:

$$\theta_{Pt-H} = \frac{a_{H_3^+O}}{a_{H_3^+O} + \frac{k_{-1}}{k_1}} = \frac{a_{H_3^+O}}{a_{H_3^+O} + \frac{k_{-10}}{k_{10}} e^{\frac{F\eta}{RT}}}$$

The net reaction rate can be written as:

$$r = k_3 a_{H_3^+O} \theta_{Pt-H} = k_{30} e^{-\frac{\alpha F\eta}{RT}} \frac{a_{H_3^+O}^2}{a_{H_3^+O} + \frac{k_{-10}}{k_{10}} e^{\frac{F\eta}{RT}}} = k_{30} e^{-\frac{(1+\alpha)F\eta}{RT}} \frac{a_{H_3^+O}^2}{a_{H_3^+O} e^{-\frac{F\eta}{RT}} + \frac{k_{-10}}{k_{10}}} \approx k_{30} \frac{k_{10}}{k_{-10}} a_{H_3^+O}^2 e^{-\frac{(1+\alpha)F\eta}{RT}}$$

$$\log_{10}(-j) = \text{const} + 2 \log_{10} \left( \frac{a_{H^+}}{3} \right) - \frac{(1 + \alpha)F\eta}{2.303RT}$$

The calculated slope of  $\log_{10}(-j)$  as a function of pH ( $-\log_{10} \left( \frac{a_{H^+}}{3} \right)$ ) is -2, again, not close to the measured value -1.16.

By comparing the experimental and calculated values, we draw the following conclusion: the addition of noble metals cannot enhance HER dynamic process merely by changing the electronic structure of B-WO<sub>2.9</sub>. This led us to realize that there might be another kinetic path on Pt/B-WO<sub>2.9</sub> surface.

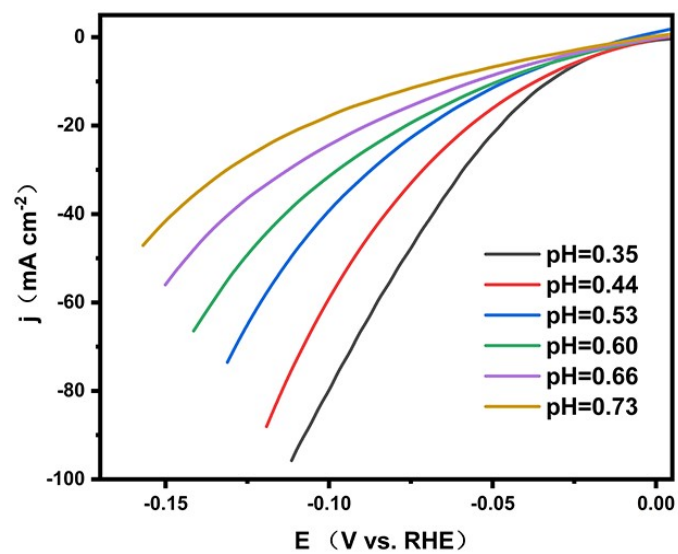


**Figure S33.** The pH-dependance measurements. LSV curves of Pt/B-WO<sub>2,9</sub> in H<sub>2</sub>SO<sub>4</sub> with different pH values.

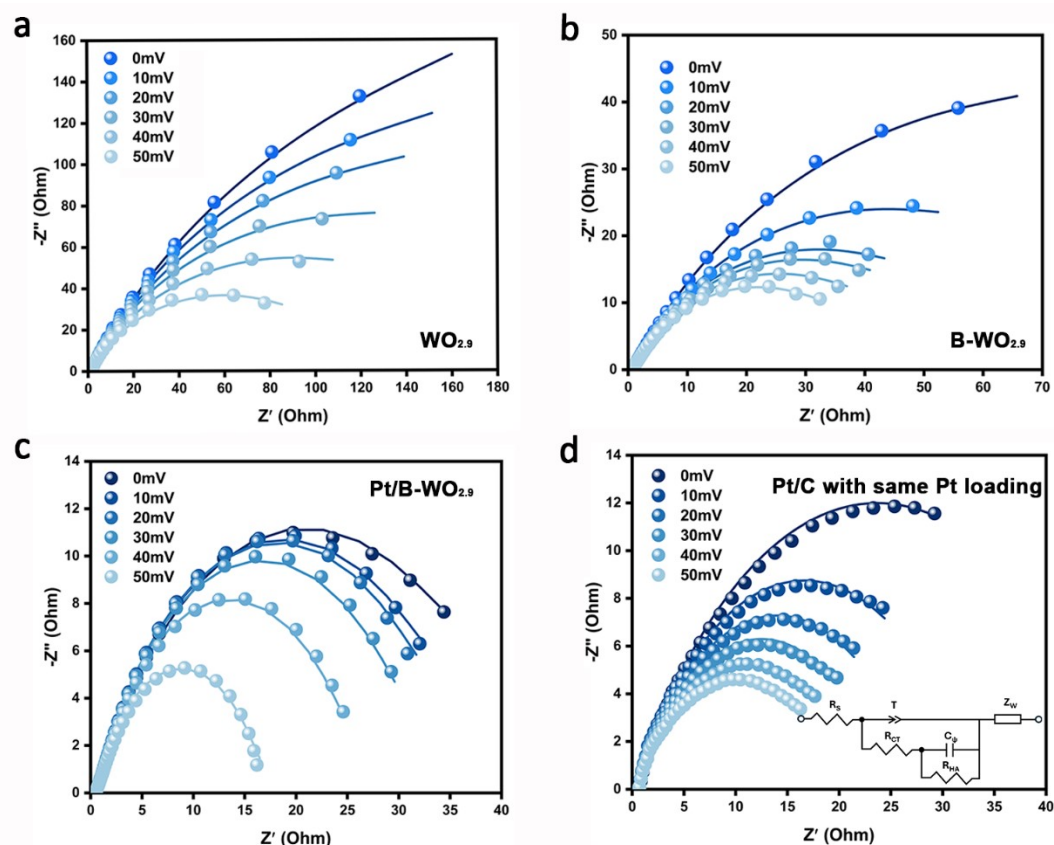


**Figure S34.** The in-situ electrochemical impedance spectroscopy (EIS) investigations in 0.5 M H<sub>2</sub>SO<sub>4</sub> saturated with H<sub>2</sub>. Nyquist plots for (a) WO<sub>2.9</sub>, (b) B-WO<sub>2.9</sub>, (c) Pt/B-WO<sub>2.9</sub> and (d) Pt/C with same Pt loading at various HER overpotentials. The spherical scatter symbol represents the experimental results, and the solid line is the simulation fitting results. The insert in (d) shows the equivalent circuit for the simulation of these four samples.  $R_s$ ,  $R_{ct}$  and  $R_{HA}$  represent the solution resistance, charge-transfer resistance, and hydrogen adsorption resistance, respectively.  $C_\phi$  represents the hydrogen adsorption pseudo-capacitance.  $Z_w$  represents the Warburg impedance, which corresponds to the diffusion resistance across the electrolyte and the catalyst layer. The fitting parameters are shown in Table S6.

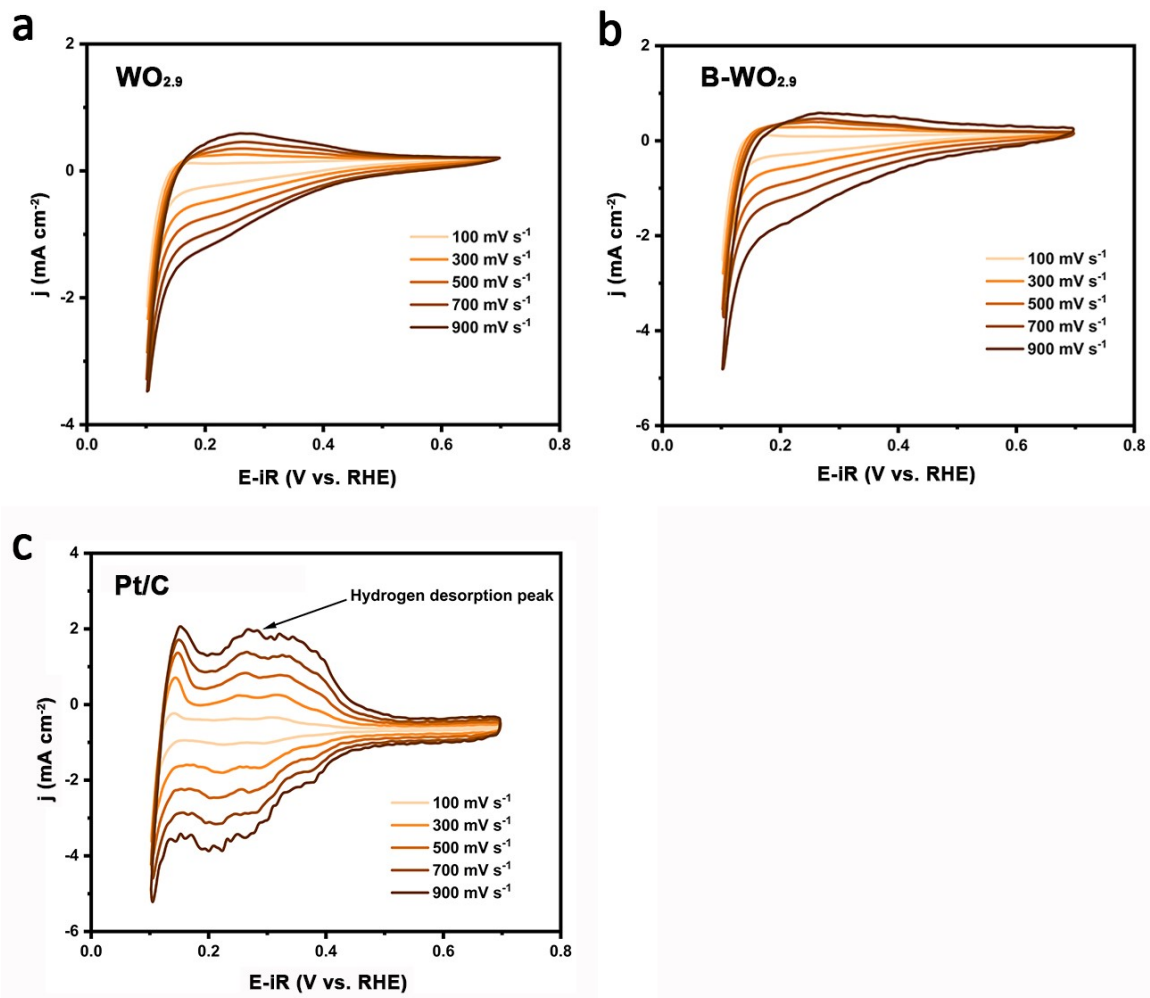


**Figure S35.** In-situ cyclic voltammetry (CV) profiles of  $\text{WO}_{2.9}$  (a),  $\text{B-WO}_{2.9}$  (b), and  $\text{Pt/C}$  (c) in 0.5 M  $\text{H}_2\text{SO}_4$  saturated with  $\text{N}_2$ . The scan rate ranging from 100 to 900  $\text{mV s}^{-1}$ .

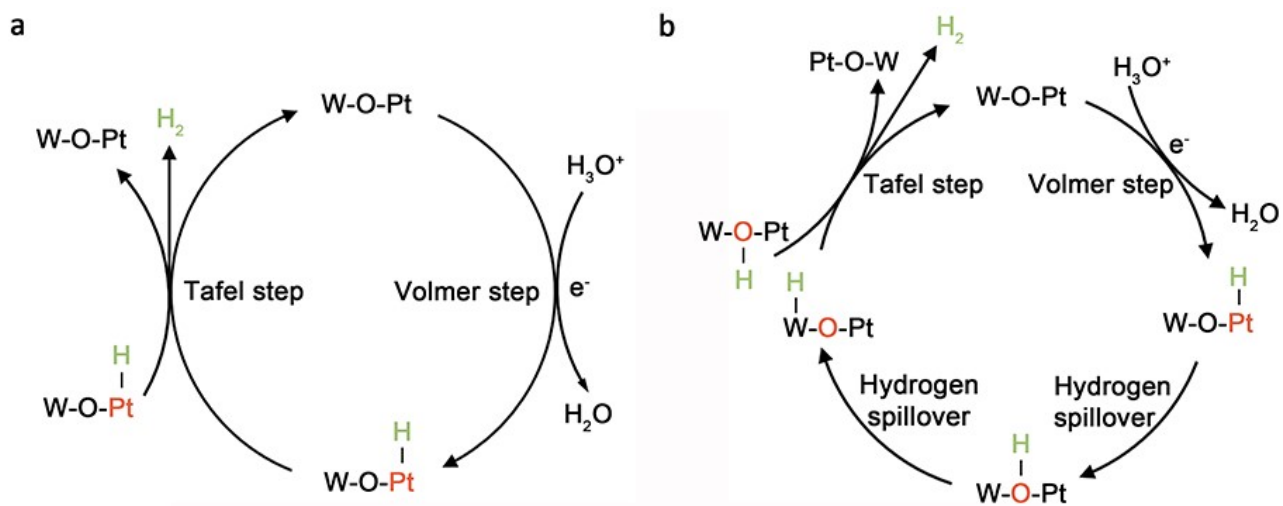
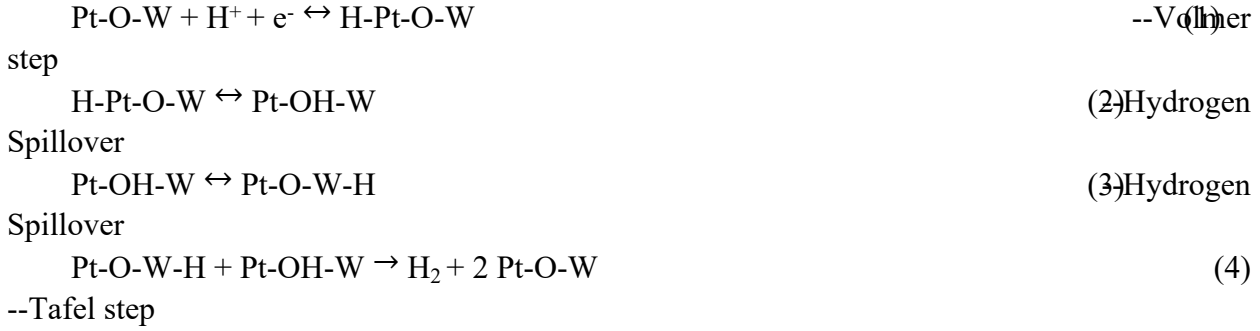


**Figure S36.** Schematic illustration of HER mechanisms. (a) Conventional Volmer-Tafel mechanism. (b) OIDEC mechanism.

**Note S7:** Calculation of OIDEK kinetic model:

Based on the single-layer adsorption model proposed by Langmuir<sup>23</sup>, (a) the surface of similar catalysts is uniform, and each active site has the same adsorption heat and thus adsorption activation energy; (b) there is no interaction between adsorbed molecules; (c) adsorption and desorption can establish dynamic equilibrium, we propose the following reaction kinetic pathway.



where the net rate of hydrogen production can be written as  $r = k_4\theta_{W-H}\theta_{O-H}$ ,  $k$  is the reaction rate constant,  $\theta$  is the percentage of active sites covered by H.

In steady state, for  $\theta_{Pt-H}$ ,

$$\begin{aligned}
 \frac{d\theta_{Pt-H}}{dt} &= k_1(1 - \theta_{Pt-H})a_{H_3^+O} - k_{-1}\theta_{Pt-H} - k_2\theta_{Pt-H}(1 - \theta_{O-H}) + \\
 k_{-2}\theta_{O-H}(1 - \theta_{Pt-H}) &= 0;
 \end{aligned}$$

For  $\theta_{O-H}$ ,

$$\begin{aligned}
 \frac{d\theta_{O-H}}{dt} &= k_2(1 - \theta_{O-H})\theta_{Pt-H} - k_{-2}(1 - \theta_{Pt-H})\theta_{O-H} - k_3\theta_{O-H}(1 - \theta_{W-H}) + \\
 k_{-3}\theta_{W-H}(1 - \theta_{O-H}) - k_4\theta_{W-H}\theta_{O-H} &= 0;
 \end{aligned}$$

And for  $\theta_{W-H}$ ,

$$\frac{d\theta_{W-H}}{dt} = k_3\theta_{O-H}(1 - \theta_{W-H}) - k_{-3}\theta_{W-H}(1 - \theta_{O-H}) - k_4\theta_{W-H}\theta_{O-H} = 0;$$

At low overpotential, clear Pt-H signals were observed in the in-situ Raman spectra (Figure 3a, 3c), while no W-H signal can be detected in the in-situ ATR-SEIRAS spectra (Figure 3e, 3f), we got  $\theta_{O-H} \approx \theta_{W-H} \ll \theta_{Pt-H}$ . From the previous literature<sup>24</sup>, we assume that the hydrogen spillover process

is reversible and the probability of occurrence is almost the same, we got  $k_1 > k_{-1} \gg k_2 \approx k_{-2} \approx k_3 \approx k_{-3}, k_4 \gg k_3$ .

Considering the positive direction of reaction (1) ( $k_1$ ) under negative potential, we assume  $a_{H_3^+O} \ll k_1^{24}$ . We can get the following approximation:

$$\theta_{Pt-H} \approx \frac{k_1 a_{H_3^+O} + k_{-2} \theta_{O-H}}{k_1 a_{H_3^+O} + k_{-1} + k_2 + k_{-2} \theta_{O-H} - k_2 \theta_{O-H}} \approx \frac{k_{10}}{k_{-10}} a_{H_3^+O} e^{-\frac{F\eta}{RT}}$$

$$\theta_{O-H} \approx \frac{k_2 \theta_{Pt-H} + k_{-3} \theta_{W-H}}{k_2 \theta_{Pt-H} + k_{-2}(1 - \theta_{Pt-H}) + k_3(1 - \theta_{W-H}) + k_{-3} \theta_{W-H} + k_4 \theta_{W-H}} \approx \frac{1}{2} (\theta_{Pt-H} + \theta_{W-H})$$

$$\theta_{W-H} \approx \frac{k_3 \theta_{O-H}}{k_3 \theta_{O-H} + k_{-3}(1 - \theta_{O-H}) + k_4 \theta_{O-H}} \approx \frac{k_3}{k_4}$$

$$r = k_4 \theta_{W-H} \theta_{O-H} = \frac{k_3}{2} (\theta_{Pt-H} + \theta_{W-H}) \approx \frac{k_3}{2} \theta_{Pt-H} = \frac{k_{30} k_{10}}{2 k_{-10}} a_{H_3^+O} e^{-\frac{(1+\alpha)F\eta}{RT}}$$

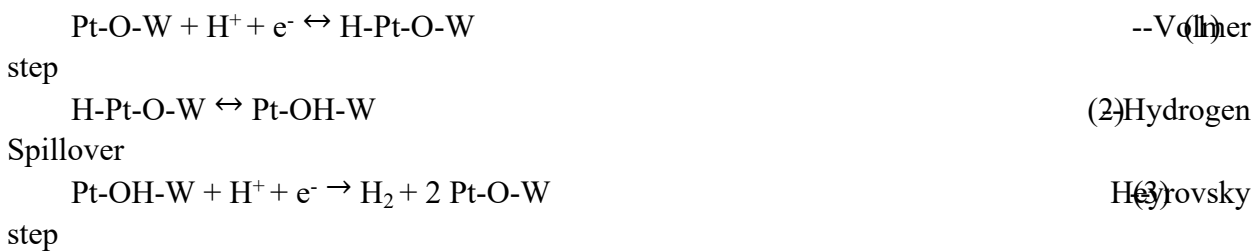
$$\log_{10}(-j) = \text{const} + \log_{10} \left( a_{H_3^+O} \right) - \frac{(1+\alpha)F\eta}{2.303RT}$$

The measured slope of  $\log_{10}(-j)$  as a function of pH ( $-\log_{10} (a_{H_3^+O})$ ) is -1.16, which is very close to our kinetic calculation of -1.

$$\text{Tafel slope} = \frac{2.303RT}{(1+\alpha)F} \approx 39 \text{ mV/dec}; \text{ The experimental value is } 33 \text{ mV/dec.}$$

The theoretical value is very close to the experimental value, so as a summary, it can be considered that our reaction kinetic path is established under the premise that the above assumptions are satisfied.

We also verify the two possible paths of the Heyrovsky step below and show why they cannot happen.



$$= k_3 a_{H_3O^+} \theta_{O-H}$$

where the net rate of hydrogen production can be written as r  
In steady state , for  $\theta_{Pt-H}$ ,

$$\frac{d\theta_{Pt-H}}{dt} = k_1(1 - \theta_{Pt-H})a_{H_3O^+} - k_{-1}\theta_{Pt-H} - k_2\theta_{Pt-H}(1 - \theta_{O-H}) + k_{-2}\theta_{O-H}(1 - \theta_{Pt-H}) = 0;$$

For  $\theta_{O-H}$ ,

$$\frac{d\theta_{O-H}}{dt} = k_2(1 - \theta_{O-H})\theta_{Pt-H} - k_{-2}(1 - \theta_{Pt-H})\theta_{O-H} - k_3\theta_{O-H}a_{H_3O^+} = 0;$$

Under the assumption of  $k_1 > k_{-1} \gg k_2 \approx k_{-2} \gg k_3$ , we got the following approximation:

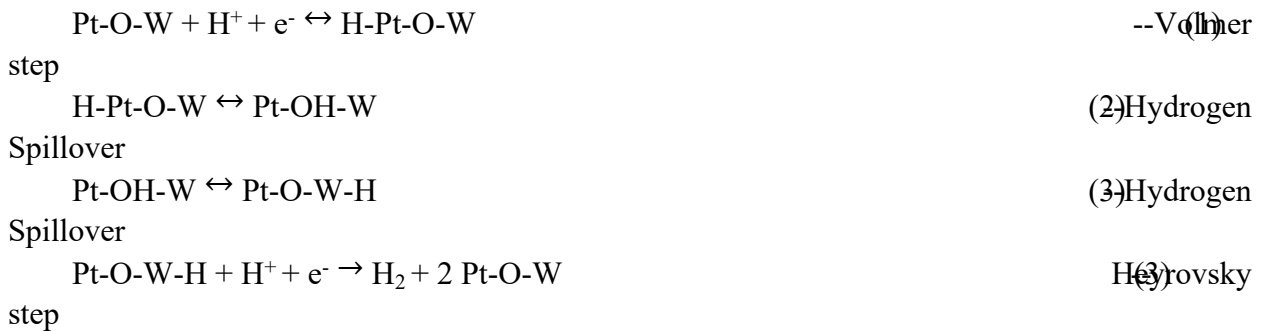
$$\theta_{Pt-H} \approx \frac{k_3 a_{H_3O^+} \theta_{O-H} + k_{-2} \theta_{O-H}}{k_2 - k_2 \theta_{O-H} + k_{-2} \theta_{O-H}} \approx \theta_{O-H}$$

$$\theta_{O-H} \approx \frac{k_2 \theta_{Pt-H} + k_{-1} \theta_{Pt-H} - k_1 a_{H_3O^+} + k_1 a_{H_3O^+} \theta_{Pt-H}}{k_2 \theta_{Pt-H} + k_{-2} - k_{-2} \theta_{Pt-H}} \approx \frac{k_1 a_{H_3O^+}}{k_{-1}}$$

$$r = k_3 a_{H_3O^+} \theta_{O-H} = \frac{k_3 k_1 a_{H_3O^+}^2}{k_{-1}} = \frac{k_{30} k_{10}}{k_{-10}} a_{H_3O^+}^2 e^{-\frac{(1+\alpha)F\eta}{RT}}$$

$$\log_{10}(-j) = \text{const} + 2 \log_{10} \left( a_{H_3O^+} \right) - \frac{(1+\alpha)F\eta}{2.303RT}$$

The calculated slope of  $\log_{10}(-j)$  as a function of pH ( $-\log_{10} \left( a_{H_3O^+} \right)$ ) is -2, which is not close to the measured value -1.16.



where the net rate of hydrogen production can be written as  $r = k_4 a_{H_3^+O} \theta_{W-H}$   
 In steady state , for  $\theta_{Pt-H}$ ,

$$\frac{d\theta_{Pt-H}}{dt} = k_1(1 - \theta_{Pt-H})a_{H_3^+O} - k_{-1}\theta_{Pt-H} - k_2\theta_{Pt-H}(1 - \theta_{O-H}) + k_{-2}\theta_{O-H}(1 - \theta_{Pt-H}) = 0;$$

For  $\theta_{O-H}$ ,

$$\frac{d\theta_{O-H}}{dt} = k_2(1 - \theta_{O-H})\theta_{Pt-H} - k_{-2}(1 - \theta_{Pt-H})\theta_{O-H} - k_3\theta_{O-H}(1 - \theta_{W-H}) + k_{-3}\theta_{W-H}(1 - \theta_{O-H}) = 0;$$

And for  $\theta_{W-H}$ ,

$$\frac{d\theta_{W-H}}{dt} = k_3\theta_{O-H}(1 - \theta_{W-H}) - k_{-3}\theta_{W-H}(1 - \theta_{O-H}) - k_4\theta_{W-H}a_{H_3^+O} = 0;$$

Under the assumption of  $k_1 > k_{-1} \gg k_2 \approx k_{-2} \approx k_3 \approx k_{-3} \gg k_4$ , we got the following approximation:

$$\theta_{Pt-H} \approx \frac{k_1 a_{H_3^+O} + k_{-2} \theta_{O-H}}{k_1 a_{H_3^+O} + k_{-1} + k_2 + k_{-2} \theta_{O-H} - k_2 \theta_{O-H}} \approx \frac{k_{10}}{k_{-10}} a_{H_3^+O} e^{-\frac{F\eta}{RT}}$$

$$\theta_{O-H} \approx \frac{k_2 \theta_{Pt-H} + k_{-3} \theta_{W-H}}{k_2 \theta_{Pt-H} + k_{-2}(1 - \theta_{Pt-H}) + k_3(1 - \theta_{W-H}) + k_{-3} \theta_{W-H}} \approx \frac{1}{2} \theta_{Pt-H}$$

$$\theta_{W-H} \approx \frac{k_3 \theta_{O-H}}{k_3 \theta_{O-H} + k_{-3}(1 - \theta_{O-H}) + k_4 a_{H_3^+O}} \approx \theta_{O-H}$$

$$r = k_4 a_{H_3^+O} \theta_{W-H} = \frac{k_4 k_1}{2 k_{-1}} a_{H_3^+O}^2 = \frac{k_{40} k_{10}}{2 k_{-10}} a_{H_3^+O}^2 e^{-\frac{(1+\alpha)F\eta}{RT}}$$

$$\log_{10}(-j) = \text{const} + 2 \log_{10} (a_{H_3^+O}) - \frac{(1+\alpha)F\eta}{2.303RT}$$

The calculated slope of  $\log_{10}(-j)$  as a function of pH ( $-\log_{10} (a_{H^+})$ ) is -2, which is not close to the measured value -1.16. Therefore, we believe that  $H_2$  is ultimately formed by the Tafel step.

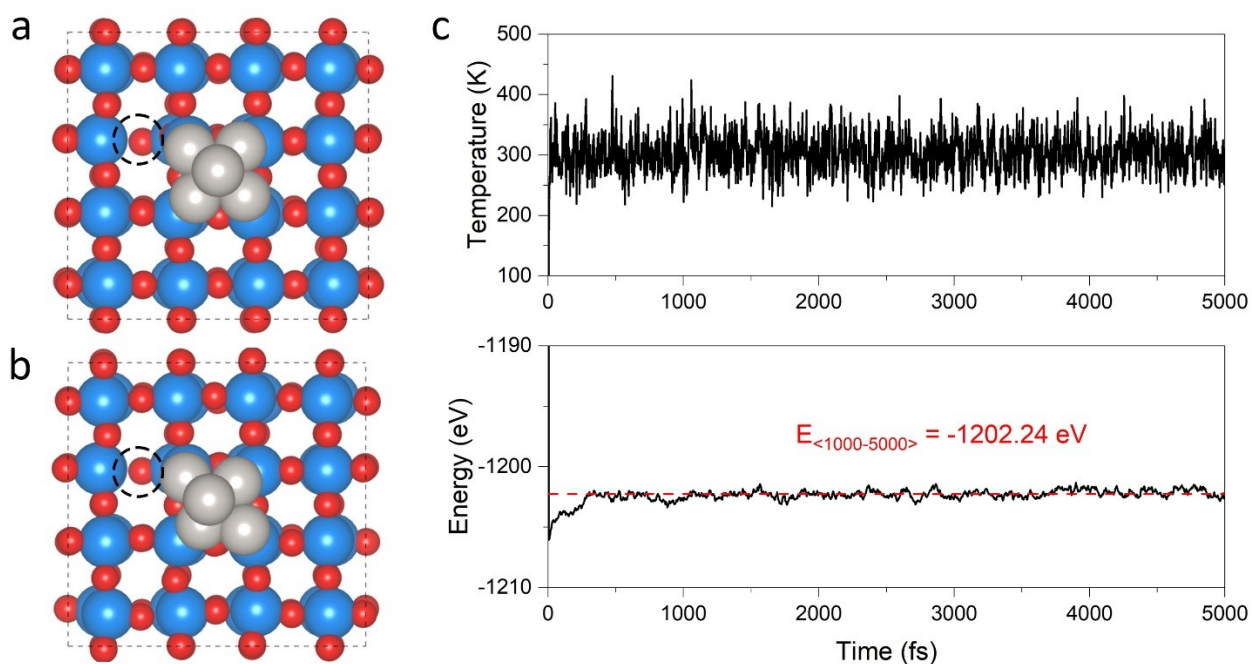


**Figure S37.** AIMD results of Pt<sub>5</sub>/O<sub>def</sub>-WO<sub>3</sub>(100). (a), (b) are the configurations of Pt<sub>5</sub>/O<sub>def</sub>-WO<sub>3</sub>(100) before and after AIMD, respectively. The black dashed circle shows the oxygen defect on the surface bridge site. The gray, blue, and red spheres represent Pt, W, and O atoms, respectively (c) shows the temperature fluctuation and energy evolution of Pt<sub>5</sub>/O<sub>def</sub>-WO<sub>3</sub>(100) during the AIMD simulation. The average energy from 1000 fs to 5000 fs is -1202.24 eV.

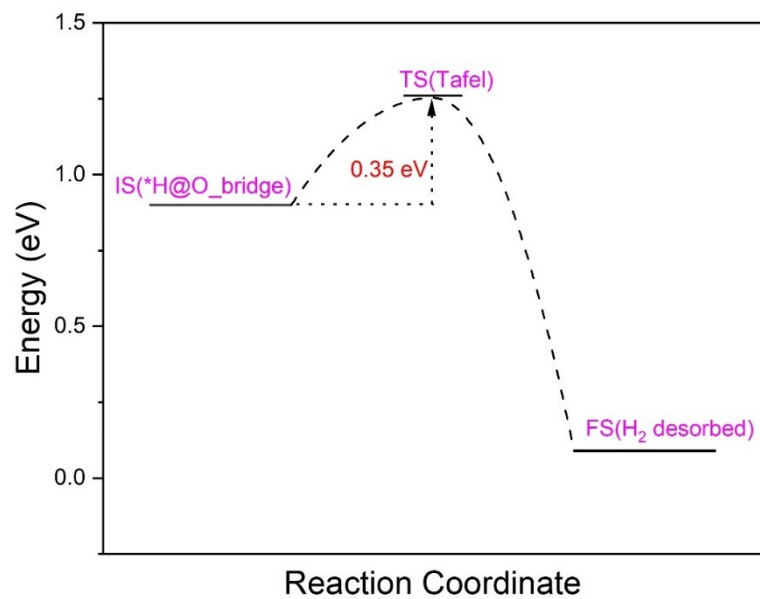


**Figure S38.** The energy diagram of Tafel process. The Tafel process happens at the end of the second  $*H$  spillover process. The transition state (TS) of Tafel process has been validated by imaginary frequency analysis (Table S6).

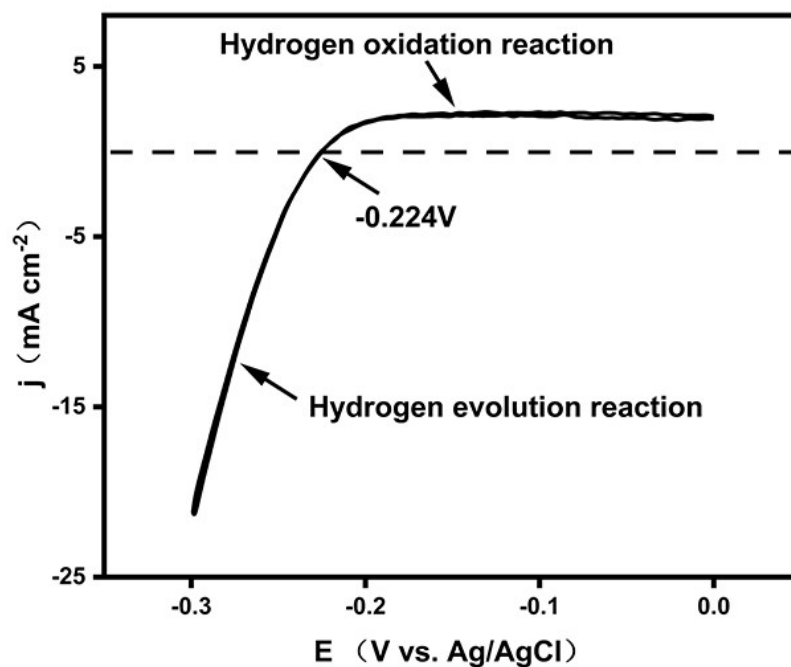


**Figure S39.** Calibration of Ag/AgCl reference electrodes in H<sub>2</sub>-saturated 0.5 M H<sub>2</sub>SO<sub>4</sub>. Pt foil as the working electrode, Pt wire as the counter electrode, Ag/AgCl as the reference electrode. CVs were performed at the scanning rate of 1 mV s<sup>-1</sup>, and the thermodynamic potential of the hydrogen electrode reaction is obtained from the average value of the two potentials when the current crossed zero, so  $E_{\text{RHE}} = E_{\text{Ag/AgCl}} + 0.224 \text{ V}$ .

**Table S1.** Structural parameters obtained from the curve-fitting analysis of the W L<sub>3</sub>-edge EXAFS spectra.

Sample	Path	<i>N</i>	<i>R</i> (Å)	$\sigma^2$ ( $\times 10^{-3}$ Å <sup>2</sup> )	$\Delta E_0$	<i>R</i> ( $\times 10^{-3}$ )
WO <sub>3</sub>	W-O <sub>1</sub>	2±0.1	2.07±0.01	3.0±0.1	5.7±1.3	0.19
	W-O <sub>2</sub>	4±0.1	1.80±0.01	6.1±0.1		
WO <sub>2.9</sub>	W-O <sub>1</sub>	1.8±0.1	2.08±0.01	4.5±0.1	-7.9±1.8	0.26
	W-O <sub>2</sub>	4±0.1	1.82±0.01	7.8±0.1		
B-WO <sub>2.9</sub>	W-O <sub>1</sub>	1.8±0.1	2.06±0.01	6.3±0.1	-0.6±1.5	0.35
	W-O <sub>2</sub>	4±0.1	1.79±0.01	7.5±0.1		
Pt/B-WO <sub>2.9</sub>	W-O <sub>1</sub>	1.9±0.1	2.03±0.01	6.3±0.1	-1.2±14.0	0.13
	W-O <sub>2</sub>	4±0.1	1.78±0.01	11.4±0.1		

*N* is the coordination number.

*R* is the distance between absorber and backscatter atoms.

$\sigma^2$  is the Debye-Waller factor value.

$\Delta E_0$  is the inner potential correction to account for the difference in inner potential between the sample and the reference compound.

*R* is the residual factor.

**Table S2.** Three independent carbon paper containing Pt/B-WO<sub>2.9</sub> with an area of 0.5 cm<sup>2</sup> were dissolved in 5 mL aqua regia, respectively. The solution concentration as measured by Inductively Coupled Plasma-Atomic Emission Spectroscopy (ICP-AES), and its corresponding mass per unit area.

<b>Concentration (ppm)</b>	<b>Mass per unit area ( mg cm<sup>-2</sup>)</b>
0.088	0.88*10 <sup>-3</sup>
0.079	0.79*10 <sup>-3</sup>
0.091	0.91*10 <sup>-3</sup>

$$0.088 \text{ mg/L} * 5 \text{ mL} / 0.5 \text{ cm}^2 = 0.88 * 10^{-3} \text{ mg cm}^{-2}$$

Average mass per unit area :

$$(0.88 * 10^{-3} + 0.79 * 10^{-3} + 0.91 * 10^{-3}) / 3 \text{ mg/ cm}^2 = 0.86 * 10^{-3} \text{ mg/ cm}^2$$

**Table S3.** HER performance of Pt/B-WO<sub>2.9</sub> and other reported metal-based catalysts in acidic medium (0.5 M H<sub>2</sub>SO<sub>4</sub>).

Catalysts	$\eta@$ (10mA cm <sup>-2</sup> )	TOF (s <sup>-1</sup> ) @overpotential (mV)	ref
Pt/B-WO <sub>2.9</sub>	36	77@100	This work
Ru@C <sub>2</sub> N	31	NA	25
CoPS film	128	NA	26
CoPS NWs	61	NA	26
CoPS NPls	48	NA	26
Metallic WO <sub>2</sub> -carbon MN	58	NA	27
A-Ni@DG	70	5.7@100	28
PtN <sub>x</sub> /TiO <sub>2</sub>	67	37.97@100	29
Co-NG	147	1.189@200	30
CoN <sub>x</sub> /C	133	0.39@100	31
MoC–Mo <sub>2</sub> C	114	1.3@250	32
Ru–FeP	62	1.5@100	33
NiCo <sub>2</sub> Px	58	0.0021@100	34
Pt <sub>1</sub> /NMHCS	40	20.18@300	35
Se-MoS <sub>2</sub> -NF	132	NA	36
Pt@PCM	105	43.6@500	37
NiN <sub>4</sub> -Cl SAs/N-C	274	0.13@300	38
Pt/f-MWCNTs	43.9	0.921@0	39
Se-MoS <sub>2</sub>	104	1.51@200	40
Li <sup>+</sup> activated WSe <sub>2</sub> NF	243	NA	41
Pt-AC/DG-X-100	52	13.98@50	42
[Mo <sub>3</sub> S <sub>13</sub> ] <sup>2-</sup>	180	3@200	43
Ru-MoS <sub>2</sub> /CNT	50	NA	44

**Table S4.** Comparison of the cost, active metal loading, and HER performance of Pt/B-WO<sub>2.9</sub> with various representative catalysts reported in literature.

Catalysts	Active metal loading ( $\mu\text{g cm}^{-2}$ )	Active metal	Prices (\$ g <sup>-1</sup> )	Cost*10 <sup>-4</sup> (\$ cm <sup>-2</sup> )	$\eta$ @ (10mA cm <sup>-2</sup> )	ref
Pt/B-WO <sub>2.9</sub>	0.86	Pt	378.15	3.26	36	This work
Ru@C <sub>2</sub> N	3.88	Ru	339.83	13.2	31	25
A-Ni@DG	3.25	Ni	15.72	0.511	70	28
Co-NG	285	Co	2.68	7.63	147	30
CoN <sub>x</sub> /C	2800	Co	2.68	75	133	31
Pt <sub>1</sub> /NMHCS	6.57	Pt	378.15	24.8	40	35
Pt/f-MWCNTs	0.914	Pt	378.15	3.45	43.9	39
Pt-AC/DG-X-100	2.77	Pt	378.15	10.47	52	42
Pt@PCM	7.95	Pt	378.15	30	105	37
[Mo <sub>3</sub> S <sub>13</sub> ] <sup>2-</sup>	10	Mo	1.08	0.23	180	43

**Table S5.** Comparison of synthesis conditions and chemical treatments for Pt/B-WO<sub>2.9</sub> and other catalysts.

Catalysts	Temperature (°C)	Time (h)	Additional processing	Organic Solvent/Compounds	Acid/Base Treatment	ref
Pt/B-WO <sub>2.9</sub>	600	2	Electrodeposition	\	\	This work
PtN <sub>x</sub> /TiO <sub>2</sub>	350	3	N <sub>2</sub> Plasma	\	\	29
Pt@PCM	800	2	\	Tetrahydrofuran	\	37
CoN <sub>x</sub> /C	900	4	\	o-Phenylenediamine	NaOH	31
A-Ni@DG	750	2	\	\	HCl	28
Pt-AC/DG	\	\	Electrodeposition	\	\	42
Co-NG	750	2	Freeze Drying	\	\	30
Pt <sub>1</sub> /NMHCS	800	2	\	\	NaOH	39
Ru-FeP	300	2	Phosphorization	\	H <sub>2</sub> SO <sub>4</sub>	33
[Mo <sub>3</sub> S <sub>13</sub> ] <sup>2-</sup>	200	2	Water Bath	Methanol	\	43

**Table S6.** The fitted parameters of the EIS data of the Pt/C, Pt/B-WO<sub>2.9</sub>, B-WO<sub>2.9</sub> and WO<sub>2.9</sub> catalysts for HER.

Catalysts	$\eta$ [mV]	$R_s$ [ $\Omega$ ]	$T$ [ $F\ s^{-1}$ ]	$n$	$R_{ct}$ [ $\Omega$ ]	$C\phi$ [mF]	$R_{HA}$ [ $\Omega$ ]	$Zw$ [ $\Omega$ ]
<b>Pt/C</b>	0	0.31031	0.000320	0.60439	46.77	0.56693	44.02	0.03422
	-10	0.31587	0.000261	0.62717	32.66	0.59026	28.46	0.04129
	-20	0.32165	0.000277	0.62253	27.42	0.73307	17.74	0.04674
	-30	0.33195	0.000326	0.60982	24.28	0.90278	11.59	0.05057
	-40	0.33099	0.000385	0.59521	21.28	1.26278	8.13	0.05664
	-50	0.33557	0.000445	0.58373	19.28	1.61675	5.24	0.06154
<b>Pt/B-WO<sub>2.9</sub></b>	0	0.49695	0.008744	0.63655	40.51	1.095	42.97	0.02907
	-10	0.53740	0.007745	0.67596	36.45	1.208	26.57	0.03121
	-20	0.55766	0.007774	0.68830	34.88	1.541	15.25	0.03241
	-30	0.55945	0.007344	0.69917	32.06	2.196	8.32	0.03417
	-40	0.58136	0.007368	0.71761	25.84	2.881	5.27	0.04067
	-50	0.56919	0.006508	0.72048	16.31	3.446	2.93	0.06179
<b>B-WO<sub>2.9</sub></b>	0	0.5528	0.010545	0.66327	140.5	0.36591	82.9	0.01793
	-10	0.56536	0.010631	0.66842	82.21	0.45525	68.44	0.02079
	-20	0.56828	0.011256	0.67575	61.07	0.57189	57.85	0.02463
	-30	0.58163	0.011346	0.6763	55.86	0.59221	49.03	0.02563
	-40	0.57822	0.011766	0.67732	48.75	0.72015	42.32	0.02819
	-50	0.5786	0.011924	0.67812	41.9	0.75972	35.84	0.03085
<b>WO<sub>2.9</sub></b>	0	0.61995	0.004794	0.71993	553.2	0.25433	525.6	0.00834
	-10	0.68057	0.004968	0.72701	404.2	0.33972	462.6	0.00864
	-20	0.58941	0.005297	0.71652	332.9	0.43546	407.5	0.00913
	-30	0.60494	0.005349	0.72941	235.2	0.46894	345.4	0.00969
	-40	0.58335	0.005623	0.71551	174.4	0.53829	287.6	0.01075
	-50	0.58196	0.005733	0.71611	116.9	0.59856	251.3	0.01287

**Table S7.** The calculated energy profiles of hydrogen spillover and Tafel process of Pt<sub>5</sub>/O<sub>def</sub>-WO<sub>3</sub>(100) with one surface O defect site. TS (Tafel) means the transition state of Tafel process.

<b>First H spillover</b>		<b>Second H spillover</b>	
<b>site</b>	<b>Energy (eV)</b>	<b>site</b>	<b>Energy (eV)</b>
Pt_top	0.00	Pt_top	0.00
Pt_bottom	0.02	Pt_bottom	0.15
O_bridge	1.01	O_bridge	0.90
W	1.63	TS(Tafel)	1.25
		H <sub>2</sub> (g)	0.09

**Table S8.** Imaginary frequencies of the transition state in Tafel process.

1 f	=	53.983957 THz	339.191205 2PiTHz	1800.710918 cm-1	223.259780 meV
2 f	=	46.149935 THz	289.968595 2PiTHz	1539.396094 cm-1	190.860859 meV
3 f	=	32.733341 THz	205.669648 2PiTHz	1091.866699 cm-1	135.374266 meV
4 f	=	31.639886 THz	198.799264 2PiTHz	1055.392949 cm-1	130.852096 meV
5 f	=	13.853086 THz	87.041504 2PiTHz	462.089185 cm-1	57.291778 meV
6 f/i	=	34.941349 THz	219.542974 2PiTHz	1165.517926 cm-1	144.505858 meV

## References

1. J. C. Dupin, D. Gonbeau, P. Vinatier and A. Levasseur, *PCCP Phys. Chem. Chem. Phys.*, 2000, **2**, 1319-1324.
2. F. Y. Yu, Z. L. Lang, L. Y. Yin, K. Feng, Y. J. Xia, H. Q. Tan, H. T. Zhu, J. Zhong, Z. H. Kang and Y. G. Li, *Nat. Commun.*, 2020, **11**, 7.
3. J. Racek, E. Kalabisova and K. Vaclavikova, Sanya, PEOPLES R CHINA, 2011.
4. D. I. Patel, S. Noack, C. D. Vacogne, H. Schlaad, S. Bahr, P. Dietrich, M. Meyer, A. Thissen and M. R. Linford, *Surf. Sci. Spectra*, 2019, **26**, 8.
5. D. T. Clark, W. J. Feast, P. J. Tweedale and H. R. Thomas, *J. Polym. Sci. Pol. Chem.*, 1980, **18**, 1651-1664.
6. T. Hussain, M. F. Al-Kuhaili, S. M. A. Durrani, A. Qurashi and H. A. Qayyum, *Int. J. Hydrog. Energy*, 2017, **42**, 28755-28765.
7. J. I. Jeong, J. H. Hong, J. H. Moon, J. S. Kang and Y. Fukuda, *J. Appl. Phys.*, 1996, **79**, 9343-9348.
8. S. Lingzhi and Z. Xu, *Adv. Mater. Res. (Switzerland)*, 2013, **699**, 194-199.
9. C. Y. Li, J. B. Le, Y. H. Wang, S. Chen, Z. L. Yang, J. F. Li, J. Cheng and Z. Q. Tian, *Nat. Mater.*, 2019, **18**, 697-+.
10. S. Balaji, Y. Djaoued, A. S. Albert, R. Bruning, N. Beaudoin and J. Robichaud, *J. Mater. Chem.*, 2011, **21**, 3940-3948.
11. D. Lampakis, D. Palles, E. Liarokapis and J. A. Mydosh, *Physica B*, 2006, **378-80**, 578-580.
12. R. L. Frost and E. C. Keeffe, *Spectroc. Acta Pt. A-Molec. Biomolec. Spectr.*, 2011, **81**, 111-116.
13. R. L. Frost and Y. F. Xi, *Spectroc. Acta Pt. A-Molec. Biomolec. Spectr.*, 2012, **91**, 314-318.
14. A. A. K. King, B. R. Davies, N. Noorbehesht, P. Newman, T. L. Church, A. T. Harris, J. M. Razal and A. I. Minett, *Sci Rep*, 2016, **6**, 6.
15. N. Vast, S. Baroni, G. Zerah, J. M. Besson, A. Polian, M. Grimsditch and J. C. Chervin, *Phys. Rev. Lett.*, 1997, **78**, 693-696.
16. S. Y. Wu, Y. Li and X. M. Chen, *J. Phys. Chem. Solids*, 2003, **64**, 2365-2368.
17. E. G. Robertson, C. D. Thompson, D. Appadoo and D. McNaughton, *PCCP Phys. Chem. Chem. Phys.*, 2002, **4**, 4849-4854.
18. C. Balazsi, M. Farkas-Jahnke, I. Kotsis, L. Petras and J. Pfeifer, *Solid State Ion.*, 2001, **141**, 411-416.
19. H. Prats and K. Chan, *PCCP Phys. Chem. Chem. Phys.*, 2021, **23**, 27150-27158.
20. T. Shinagawa, A. T. Garcia-Esparza and K. Takanabe, *Sci Rep*, 2020, **10**, 1.
21. A. J. Bard and L. R. Faulkner, *Electrochemical Methods: Fundamentals and Applications, 2nd Edition*, John Wiley & Sons Inc., New York 2001.
22. E. Kochanski, *Journal of Organometallic Chemistry*, 1994, **466**, C7.
23. I. Langmuir, *J. Am. Chem. Soc.*, 1917, **39**, 1848-1906.
24. L. L. Zhu, H. P. Lin, Y. Y. Li, F. Liao, Y. Lifshitz, M. Q. Sheng, S. T. Lee and M. W. Shao, *Nat. Commun.*, 2016, **7**, 7.
25. J. Mahmood, F. Li, S. M. Jung, M. S. Okyay, I. Ahmad, S. J. Kim, N. Park, H. Y. Jeong and J. B. Baek, *Nat. Nanotechnol.*, 2017, **12**, 441-446.
26. M. Caban-Acevedo, M. L. Stone, J. R. Schmidt, J. G. Thomas, Q. Ding, H. C. Chang, M. L. Tsai, J. H. He and S. Jin, *Nat. Mater.*, 2015, **14**, 1245-1251.
27. R. Wu, J. F. Zhang, Y. M. Shi, D. Liu and B. Zhang, *J. Am. Chem. Soc.*, 2015, **137**, 6983-6986.
28. L. Z. Zhang, Y. Jia, G. P. Gao, X. C. Yan, N. Chen, J. Chen, M. T. Soo, B. Wood, D. J. Yang, A. J. Du and X. D. Yao, *Chem*, 2018, **4**, 285-297.
29. X. Cheng, Y. Lu, L. R. Zheng, Y. T. Cui, M. Niibe, T. Tokushima, H. Y. Li, Y. F. Zhang, G. Chen, S. R. Sun and J. J. Zhang, *Nano Energy*, 2020, **73**, 10.
30. H. L. Fei, J. C. Dong, M. J. Arellano-Jimenez, G. L. Ye, N. D. Kim, E. L. G. Samuel, Z. W. Peng, Z. Zhu, F. Qin,

- J. M. Bao, M. J. Yacaman, P. M. Ajayan, D. L. Chen and J. M. Tour, *Nat. Commun.*, 2015, **6**, 8.
31. H. W. Liang, S. Bruller, R. H. Dong, J. Zhang, X. L. Feng and K. Mullen, *Nat. Commun.*, 2015, **6**, 8.
32. W. Liu, X. T. Wang, F. Wang, K. F. Du, Z. F. Zhang, Y. Z. Guo, H. Y. Yin and D. H. Wang, *Nat. Commun.*, 2021, **12**, 10.
33. H. S. Shang, Z. H. Zhao, J. J. Pei, Z. L. Jiang, D. N. Zhou, A. Li, J. C. Dong, P. F. An, L. R. Zheng and W. X. Chen, *J. Mater. Chem. A*, 2020, **8**, 22607-22612.
34. R. Zhang, X. X. Wang, S. J. Yu, T. Wen, X. W. Zhu, F. X. Yang, X. N. Sun, X. K. Wang and W. P. Hu, *Adv. Mater.*, 2017, **29**, 7.
35. P. Y. Kuang, Y. R. Wang, B. C. Zhu, F. J. Xia, C. W. Tung, J. S. Wu, H. M. Chen and J. G. Yu, *Adv. Mater.*, 2021, **33**, 9.
36. Z. L. Zheng, L. Yu, M. Gao, X. Y. Chen, W. Zhou, C. Ma, L. H. Wu, J. F. Zhu, X. Y. Meng, J. T. Hu, Y. C. Tu, S. Wu, J. Mao, Z. Q. Tian and D. H. Deng, *Nat. Commun.*, 2020, **11**, 10.
37. H. B. Zhang, P. F. An, W. Zhou, B. Y. Guan, P. Zhang, J. C. Dong and X. W. Lou, *Sci. Adv.*, 2018, **4**, 9.
38. M. Li, M. M. Wang, D. Y. Liu, Y. Pan, S. J. Liu, K. A. Sun, Y. J. Chen, H. Y. Zhu, W. Y. Guo, Y. P. Li, Z. M. Cui, B. Liu, Y. Q. Liu and C. G. Liu, *J. Mater. Chem. A*, 2022, **10**, 6007-6015.
39. J. P. Ji, Y. P. Zhang, L. B. Tang, C. Y. Liu, X. H. Gao, M. H. Sun, J. C. Zheng, M. Ling, C. D. Liang and Z. Lin, *Nano Energy*, 2019, **63**, 8.
40. J. Hu, B. L. Huang, C. X. Zhang, Z. L. Wang, Y. M. An, D. Zhou, H. Lin, M. K. H. Leung and S. H. Yang, *Energy Environ. Sci.*, 2017, **10**, 593-603.
41. D. A. Henckel, O. M. Lenz, K. M. Krishnan and B. M. Cossairt, *Nano Lett.*, 2018, **18**, 2329-2335.
42. Q. Q. Cheng, C. G. Hu, G. L. Wang, Z. Q. Zou, H. Yang and L. M. Dai, *J. Am. Chem. Soc.*, 2020, **142**, 5594-5601.
43. J. Kibsgaard, T. F. Jaramillo and F. Besenbacher, *Nat. Chem.*, 2014, **6**, 248-253.
44. X. Zhang, F. Zhou, S. Zhang, Y. Y. Liang and R. H. Wang, *Adv. Sci.*, 2019, **6**, 7.